



**Australian Government**  
**Department of Defence**  
Defence Science and  
Technology Organisation

# Simulation of a Wing-Body Junction Experiment using the Fluent Code

*D.A. Jones and D.B. Clarke*

**Maritime Platforms Division**

Platforms Sciences Laboratory

DSTO-TR-1731

## **ABSTRACT**

Numerical simulations are performed using the Fluent Computational Fluid Dynamics code and the various turbulence models to simulate the horseshoe vortex formed in a typical wing-junction turbulent flow experiment. Simulations were conducted using the renormalizable  $k-\varepsilon$  model, the Reynolds Stress Model, the V2F model, the Spalart-Allmaras model and the  $k-\omega$  model. The calculated results were compared with experimental results obtained from an extensive database available on the internet [3]. The realizable  $k-\varepsilon$  model was noticeably less accurate than all other models in simulating the mean velocity components, while the remaining models all displayed similar levels of accuracy. None of the models were able to accurately simulate the correct behaviour of the mean kinetic energy as a function of position. The V2F model however came closest to predicting the correct behaviour, and offers the best combination of computational accuracy, computational efficiency, and ease of use.

## **RELEASE LIMITATION**

*Approved for public release*

*Published by*

*DSTO Platforms Sciences Laboratory  
506 Lorimer St  
Fishermans Bend, Victoria 3207 Australia*

*Telephone: (03) 9626 7000*

*Fax: (03) 9626 7999*

*© Commonwealth of Australia 2005*

*AR-013-426*

*June 2005*

**APPROVED FOR PUBLIC RELEASE**

# Simulation of a Wing-Body Junction Experiment using the Fluent Code

## Executive Summary

The horseshoe vortex formed at the sail/hull junction on a submarine has a number of characteristics which are undesirable for efficient submarine performance. These include the generation of unwanted noise, increased local surface shear stress and drag, as well as incoherent fluid loading on the propellers which can lead to narrowband sound generation. An increased understanding of the fluid behaviour in these types of flows would lead to improvements in submarine performance through increased stealth, reduced vulnerability and improved hydrodynamic performance.

A detailed experimental study of the horseshoe vortex formed in the vicinity of the nose of a modified NACA 0020 airfoil in a fully developed turbulent boundary layer has recently been reported in the literature by Devenport and Simpson. The data obtained in this experiment are of a particularly high quality and are readily available in electronic format on the internet. This report documents results obtained using the Fluent Computational Fluid Dynamics code to simulate the horseshoe vortex formed in this experiment. It forms part of an overall study aimed at understanding and characterizing the vortex near the sail and at downstream locations so that designs may be implemented to minimize the adverse effects of the vortex structure on submarine performance.

Simulations were conducted using five different turbulence models contained within the code to ascertain the effectiveness of each model. The calculated results were compared with experimental results obtained from the database available on the internet. The simulations showed that the realizable  $k-\varepsilon$  model was noticeably less accurate than all other models in simulating the mean velocity components. The remaining models, which consisted of the Reynolds Stress Model, V2F model, Spalart-Allmaras model and the  $k-\omega$  model, all displayed similar levels of accuracy. None were able to accurately simulate the correct behaviour of the mean kinetic energy as a function of position close to boundaries, although all were able to simulate the time-averaged velocity components at most locations within the flow to within an acceptable accuracy. The V2F model came closest to predicting the correct behaviour overall, and offers the best combination of computational accuracy, computational efficiency, and ease of use for further studies of this type of turbulent flow.

## Authors

### **David A. Jones**

Maritime Platforms Division

*Dr. David A. Jones obtained a B.Sc. (Hons) and Ph.D. in Theoretical Physics from Monash University in 1973 and 1976 respectively. He joined the then Materials Research Laboratories in 1983 after postdoctoral positions at the University of Strathclyde, Glasgow; Queen Mary College, London University, and the University of New South Wales, Sydney. During 1987/88 he was a visiting scientist at the Laboratory for Computational Physics and Fluid Dynamics at the Naval Research Laboratory, Washington, DC. He has authored 80 journal articles and technical reports and given more than 60 presentations at scientific meetings. His research has covered a variety of areas including polymer dynamics, the application of chaos theory to atomic and molecular physics, laser-plasma interaction theory, warhead design, air blast, detonation physics and computational fluid dynamics. He is currently using new Lagrangian vorticity methods to model hydrodynamic flow around underwater vehicles.*

---

### **David B. Clarke**

Maritime Platforms Division

*David Clarke commenced work in the Maritime Operations Division (MOD) at AMRL in 1988 after completing a BSc at Sydney University. His work in MOD focused on magnetic sensors and instrumentation. He obtained a Graduate Diploma in computer engineering from RMIT in 1996. In 1998 he joined the Maritime Platforms Division to work on the hydrodynamics of underwater vehicles. His work on underwater vehicles has encompassed experiment, empirical and computational hydrodynamics.*

---

## Glossary

CFD	Computational Fluid Dynamics
Fluent	Commercial CFD software
RANS	Reynolds Averaged Navier Stokes Equations
LES	Large Eddy Simulation
RSM	Reynolds Stress Model
Re	Reynolds number. $Re = \rho UL / \mu$
C <sub>p</sub>	Pressure coefficient. $C_p = \text{Pressure} / (0.5 \rho U^2)$
L	Characteristic body length.
$\rho$	Fluid density
$\mu$	Fluid viscosity
U	x- component of mean fluid velocity
V	y- component of mean fluid velocity
W	z- component of mean fluid velocity
U <sub>ref</sub>	Initial reference speed upstream of the flow
k	Turbulent kinetic energy
$\varepsilon$	Rate of dissipation of the turbulent kinetic energy
$\omega$	Defined most simply by $\omega = \varepsilon / k$
$\nu_T$	Turbulent viscosity
$y^+$	Wall normal distance normalized by friction velocity and viscosity
u	x-component of rapidly varying part of fluid velocity
v	y-component of rapidly varying part of fluid velocity
w	z -component of rapidly varying part of fluid velocity
v	component of the fluctuating velocity normal to a time-averaged streamline

# Contents

1. INTRODUCTION .....	1
2. THE DEVENPORT-SIMPSON EXPERIMENT .....	2
3. PREVIOUS COMPUTATIONAL STUDIES .....	3
4. THE FLUENT CODE.....	5
4.1 Pressure-Velocity Coupling .....	6
4.2 Spatial Discretization .....	6
5. TURBULENCE MODELS .....	7
6. COMPUTATIONAL GRID .....	8
7. SIMULATION RESULTS .....	10
7.1 $k-\varepsilon$ Model.....	10
7.2 Reynolds Stress Model .....	17
7.3 V2F Model .....	21
7.4 Spalart-Allmaras Model .....	25
7.5 $k-\omega$ Model.....	29
8. GRID INDEPENDENCE.....	33
9. DISCUSSION AND CONCLUSION .....	42
10. ACKNOWLEDGEMENTS.....	42
11. REFERENCES .....	43

# 1. Introduction

The Hydrodynamics Group within Maritime Platforms Division (MPD) performs computational fluid dynamics (CFD) studies on underwater flow problems relevant to submarine design. These studies examine and aim to improve the performance of these platforms through increased stealth, reduced vulnerability and improved hydrodynamic performance. Problems of interest involve the simulation of flow around a manoeuvring submarine, hydrofoil studies, hull/propeller interactions, viscous bluff body modelling, stores release modelling, and the study of the horseshoe vortex formed in the boundary layer at the hull/sail junction. These studies are carried out using a variety of CFD codes including the finite volume codes Fluent [1] and CFX [2].

The horseshoe vortex formed at the sail/hull junction on a submarine has a number of characteristics which are undesirable for efficient submarine performance. The vortex is subject to large-scale low-frequency bistable unsteadiness which appears to be generated in the nose region and which leads to the generation of unwanted noise. The vortex entrains high-momentum free-stream fluid into the corner between the hull and sail and greatly increases the local surface shear stresses and drag. The trailing legs of the vortex persist very far downstream of the sail and can maintain coherence as they are ingested into the propellers. This provides a source of unsteady loading, whose adverse side effect may be narrowband sound generation.

Devenport and Simpson [4] carried out a detailed study of a horseshoe vortex in the vicinity of the nose of a modified NACA 0020 airfoil for a fully developed turbulent boundary layer and were the first to report the bistable nature of the flow. Fleming et al. [5], Olcman and Simpson [6] and Devenport et al. [7] conducted further experiments on the same wing geometry to further elucidate details on the formation and structure of the vortex near the appendage. The velocity field downstream of the appendage has not been studied to the same extent however, and to address this shortfall Anderson and Huyer [8] recently used particle image velocimetry (PIV) to measure the full three-dimensional mean and turbulent velocity field at various stations downstream of a standard NACA 0020 airfoil.

This report documents results obtained using the Fluent code to simulate the horseshoe vortex formed in the Devenport-Simpson experiment [4]. It forms part of an overall study aimed at understanding and characterizing the vortex near the sail and at downstream locations so that designs may be implemented to minimize the adverse effects of the vortex structure on submarine performance. The advantages of studying this particular experiment are the extensive set of high-quality measurements obtained, the ready availability of this data in electronic format [3] and the detail with which the turbulent boundary layer in the approach flow has been characterised.

## 2. The Devenport-Simpson Experiment

Devenport and Simpson [4] studied the behaviour of a turbulent boundary layer on a flat plate as it encountered the nose of a cylindrical wing mounted normal to the plate. The wing cross-section consisted of a 3:2 elliptical nose (with its major axis aligned with the chord) and a NACA 0020 tail joined at the maximum thickness. The chord length was 30.5 cm, maximum thickness 7.17 cm and the height was 22.9 cm. The wing was mounted on the test wall of an open-circuit type wind tunnel powered by a centrifugal blower. The test section was 91 cm wide and 25.5 cm high. The boundary layer on the test wall was tripped by a 0.63 cm high step prior to entering the test section so that the inlet conditions were clean and well defined. The shape of the wind tunnel leading into the test section was such that the streamwise pressure gradient was effectively zero, thus producing an equilibrium turbulent boundary layer on the test wall. The turbulence intensity was 0.2% at the reference speed ( $U_{ref}$ ) of 27 m/s and the value of the Reynolds number, based on momentum thickness, was 6700. Figure 1. shows a schematic of the test geometry.

A right-handed coordinate system was used where  $X$  is in the direction of the free-stream flow,  $Y$  is normal to the flat plate and  $Z$  is normal to the wing symmetry plane. The origin of the coordinate system is at the upstream foot of the wing and  $T$  is the maximum thickness of the wing. The corresponding time-averaged velocity vectors are denoted by  $U, V, W$  and the instantaneous velocities by  $u, v, w$ . A three-component laser Doppler velocimeter was used to measure all non-zero mean-velocity and Reynolds-stress components at eleven stations in the plane of symmetry upstream of the wing. The most upstream station was located at  $X/T = -0.86$  and the closest station to the wing was located at  $X/T = -0.05$ . At each station measurements were made along a line in the  $Y$  direction covering the range  $0.001 < Y/T < 1.0$ .

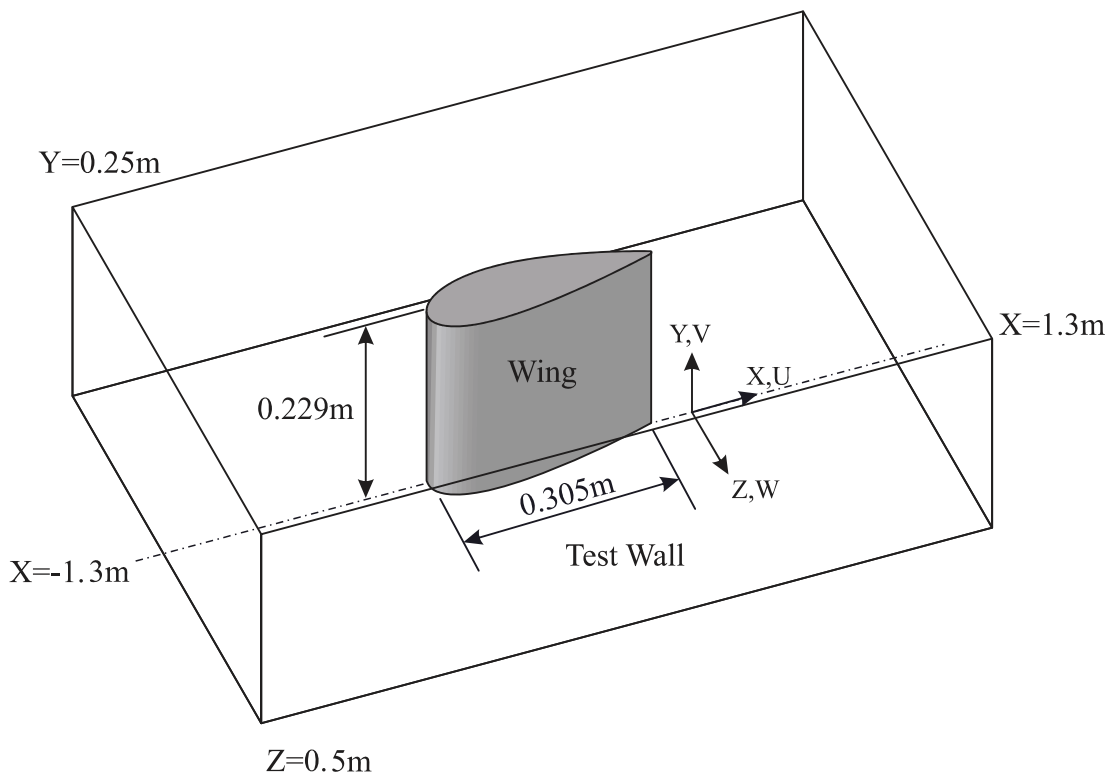


Figure 1. Perspective view of the wing-body junction.



The adverse pressure gradient in the streamwise direction imposed by the presence of the wing causes the approaching boundary layer to separate and form a horseshoe vortex which wraps around the wing. The experiment by Devenport and Simpson studied both the time-dependent and time-averaged turbulence structure near the nose of the wing-body junction. Their time-averaged velocity measurements showed a single vortex, roughly elliptical in shape, centred near  $X/T = -0.2$ ,  $Y/T = 0.05$ . The vortex generated an intense backflow with a maximum mean velocity of  $0.48U_{ref}$  and then decelerated to the separation point at  $X/T = -0.47$ . From the most upstream station to the vicinity of the separation point the measurements showed a flow developing in a manner similar to that of a two-dimensional turbulent boundary layer in an adverse pressure gradient. In the vicinity of the junction vortex however, between  $X/T = -0.3$  and  $-0.15$ , the profiles of the mean and turbulence quantities ceased to bear much resemblance to those in an adverse pressure gradient. In this region the turbulence stresses were much greater and reached values many times larger than those normally observed in turbulent flows. Examination of the time-dependent data showed that these large stresses were associated with bimodal (double-peaked) histograms of velocity fluctuations produced by a bistable velocity variation. Figure 2 shows a schematic of the mean-time velocity vectors in the plane of symmetry which illustrate the overall nature of the flow.

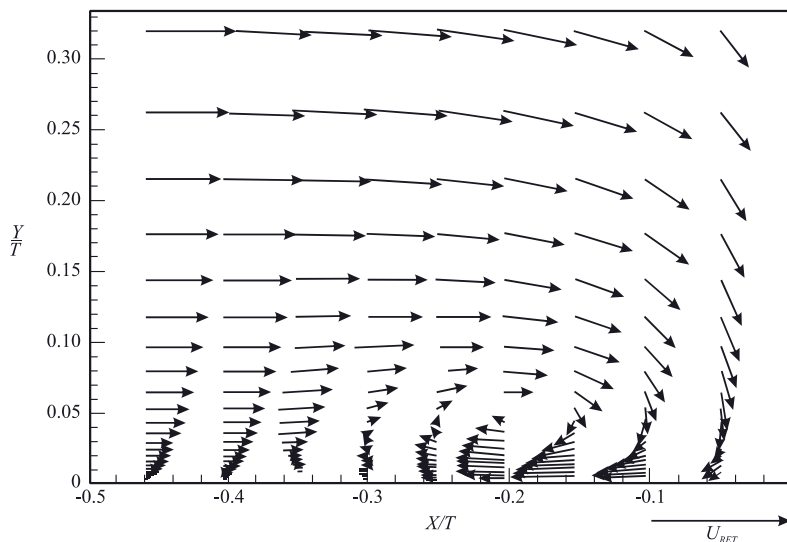


Figure 2. Mean-time velocity vectors in the plane of symmetry

Simpson [9] has discussed the time-dependent nature of the flow in the junction region in detail and summarises much of the experimental work on such systems prior to the detailed experiments of Devenport and Simpson. Initially one large horseshoe vortex exists in the junction region. As this vortex is stretched and weakened a secondary separation vortex is formed downstream of the separation and sometimes even tertiary vortices can be formed. These vortices appear to merge with the original weakened vortex at some stage and temporarily strengthen it, then the whole structure becomes unstable and is replaced by a new large-scale horseshoe vortex and the cycle repeats, although the process never becomes periodic.

### 3. Previous Computational Studies

Apsley and Leschziner [10] reported the results of a computational study of the predictive performance of twelve turbulence models, within three distinctly different classes, for the wing-body junction flow experimentally studied by Devenport and Simpson [4]. The turbulence models consisted of five linear eddy viscosity models (including variants of both the  $k-\epsilon$  and  $k-\omega$  models),

three non-linear eddy viscosity models (all of the  $k$ - $\varepsilon$  type), and four Reynolds Stress Models. The computations were performed as part of a collaborative turbulence-model-validation study involving six partners: UMIST, Loughborough University, BAE Systems, DERA, ARA and Rolls-Royce Aeroengines. Model performance was judged by comparing solutions with experimental data for pressure fields on the plane wall and around the aerofoil; for velocity, turbulence energy, shear stress and streamwise normal stress in the upstream symmetry plane; and for velocity, turbulence energy and shear stress in cross-flow planes downstream of the aerofoil leading edge. The main finding of the study was that Reynolds Stress Models offered predictive advantages over the other models examined, especially in terms of the far-field structure of the horseshoe vortex, although no model achieved close agreement with the experimental data in respect of both mean flow and turbulence quantities.

Parneix et al. [11] used the V2F turbulence model to simulate three complex three-dimensional turbulent flows: the infinitely swept bump, flow in a U-bend, and the appendage-body junction flow of Devenport and Simpson [4]. The V2F model makes use of the standard  $k$ - $\varepsilon$  model but extends it by incorporating near-wall turbulence anisotropy and non-local pressure-strain effects, while retaining a linear eddy viscosity assumption. It uses fewer equations than a full Reynolds Stress Model and is more numerically robust than these models. The V2F simulation was able to accurately calculate the separation location as well as the intensity of the back-flow. The computed U and V profiles in the symmetry plane showed excellent agreement with experiment. In contrast with all the  $k$ ,  $\varepsilon$  and RSM models surveyed by Apsley and Leschziner [10], the V2F model was also able to accurately simulate the location, shape and size of the region where the high levels of turbulence existed, and the calculated values for  $k$  were only about 30% lower than the experimental values.

Rodi et al. [12] surveyed the results of computations submitted to two ERCOFTAC Workshops on Turbulent Flow Calculations for five test cases, including the Devenport-Simpson experiment. The calculations were made using a wide variety of turbulence models including the standard  $k$ - $\varepsilon$  model with wall functions, various low-Reynolds-number versions of the  $k$ - $\varepsilon$  model, the RNG version of the  $k$ - $\varepsilon$  model, various non-linear versions, the  $k$ - $\omega$  model, various versions of Reynolds-stress models and an algebraic stress model. The general conclusion for all the test cases considered was that the more complex Reynolds-stress models and intermediate algebraic-stress and non-linear  $k$ - $\varepsilon$  models were not consistently better than the simpler linear eddy viscosity models for the practically relevant mean quantities, but in some cases they were found to give superior predictions of the details of the turbulence quantities.

For the specific case of the Devenport-Simpson experiment five calculations used versions of the  $k$ - $\varepsilon$  model and one used a Reynolds-stress model. All of the calculations reproduced reasonably well the pressure distributions on the ground plate and the wing as well as the general flow pattern, although for most models the size of the vortex was predicted to be too small, particularly for the RSM model. The strength of the horseshoe vortex as it swept around the wing was also under predicted by all the models. Experimentally the highest turbulent kinetic energy occurs in the centre of the vortex. However all the calculations, except those using the RNG version of the  $k$ - $\varepsilon$  model, predicted the maximum value of  $k$  to be very close to the corner, with excessive production of  $k$  in the stagnation region in front of the leading edge. This is a well known problem with the standard  $k$ - $\varepsilon$  model, and also occurred with the RSM model. Only the RNG version of the  $k$ - $\varepsilon$  model did not have this problem and predicted the maximum value of  $k$  in the vortex core, although with a much smaller value than in the experiment.

Chen [13] analysed the performance of two turbulence models: a two-layer isotropic eddy viscosity model and a near-wall Reynolds-stress model. The RSM model is a low Reynolds number extension of the high Reynolds number model of Speziale et al. [14] which is valid all the way to

solid walls. The calculations clearly demonstrated the superior performance of the RSM model over the simpler isotropic eddy viscosity model. In particular, the RSM model successfully resolved the detailed turbulence structures associated with the development of the appendage boundary layer, the formation of the spiral primary horseshoe vortex and the corner secondary horseshoe vortex, and the evolution of both vortices around the appendage/flat-plate junction.

Fu et al. [15] studied the behaviour of a standard linear eddy viscosity with two quadratic non-linear eddy viscosity models: the Gatski-Speziale model [16], and a realizable version of the Gatski-Speziale model due to Fu et al. [17]. All three models gave close results for the mean flow velocities, but significant differences appeared in the Reynolds stresses. The two non-linear eddy viscosity models provided overall better performance than the linear version, with the renormalized version providing marginally better performance. The three-dimensional boundary layer skewness was not calculated correctly however and Fu et al. concluded that three-dimensional anisotropic effects could not be modelled using a quadratic non-linear eddy viscosity model.

## 4. The Fluent Code

Fluent Version 6.1 is a CFD computer code developed and marketed by Fluent Inc. [1]. The code solves the equations for conservation of mass, momentum, energy and other relevant fluid variables using a Finite Volume technique. First the fluid domain is divided into a large number of discrete control volumes (also known as cells) using a pre-processor code which creates a computational mesh on which the equations can be solved. The meshing software available with Fluent is called Gambit. This software can create a two-dimensional (2D) surface mesh using triangular or quadrilateral elements, or a three-dimensional (3D) volume mesh using a combination of hexahedral, tetrahedral or prism elements.

Once the fluid domain has been meshed the governing equations (in integral form) for the conservation of mass, momentum, energy and any other relevant variables are applied to each discrete control volume and used to construct a set of non-linear algebraic equations for the discrete dependent variables. Fluent then solves the complete set of coupled equations for all the control volumes on the mesh using either a segregated solver or a coupled solver. In all the calculations reported here only the segregated solver has been used. In this approach the governing equations are solved sequentially. Since these equations are non-linear they first have to be linearized. This can be done either implicitly or explicitly, although when using the segregated solution method within Fluent the code automatically linearises each discrete governing equation implicitly with respect to that equation's dependent variable. This produces a scalar system of equations containing only one equation per computational cell. A point implicit (Gauss-Siedel) linear equation solver is then used in conjunction with an algebraic multigrid (AMG) method to solve the resultant scalar system of equations for the dependent variable in each cell. Since the equations are non-linear several iterations of the solution loop must be performed before a converged solution is obtained.

The segregated solver thus solves for a given fluid variable (for example  $U$  – the  $x$  component of velocity) by considering all cells at a single time. It then solves for the next fluid variable (for example  $V$  – the  $y$  component of velocity) by again considering all cells at the same time. Each iteration of the solution loop thus consists of the following steps:

1. The values of the fluid variables at the cell centres are updated based on the current solution values.

2. The U, V and W velocity components of the momentum equation are each solved in turn using the current values for the pressure and the mass fluxes through each of the cell faces.
3. The pressure correction equation (a form of the continuity equation) is then solved to obtain the necessary corrections to the pressure and velocity fields so that the continuity equation is satisfied.
4. Where appropriate, additional scalar equations (such as those describing transport of turbulence quantities) are solved.
5. A check for convergence is made.
6. The above steps are repeated until the convergence criteria are met (all residuals less than  $10^{-6}$ )

#### 4.1 Pressure-Velocity Coupling

As described above, an equation for each component of the momentum equation and then the continuity equation are solved sequentially. Once the three components of velocity have been calculated for each cell using this sequential system the velocities may not satisfy the continuity equation and so a “Poisson-type” equation for a pressure correction is derived from the continuity equation and the linearized momentum equations. This pressure correction equation is then solved to obtain the necessary corrections to the pressure and velocity fields such that continuity is satisfied.

Although the pressure variable appears in each of the component momentum equations each of these equations is solved by treating the relevant component of velocity as the unknown variable and the pressure field in the equation is taken to be that from the previous iteration. In this sequential procedure the continuity equation is used as an equation for the pressure. However pressure does not appear explicitly in the continuity equation for incompressible flows (which are the only flows considered in this report) and so a procedure must be devised to introduce pressure into this equation. Fluent provides methods based on the SIMPLE (Semi-Implicit Method for Pressure-Linked Equations) family of algorithms to do this [37].

The basic SIMPLE algorithm uses a relationship between velocity and pressure corrections to enforce mass conservation and to obtain the pressure field. The SIMPLER algorithm (SIMPLE-Consistent) is a variation of the SIMPLE algorithm which uses a more refined expression for the variable flux through each of the cell faces and which can accelerate convergence in some problems where the pressure-velocity coupling is the main deterrent to obtaining a solution [38]. The PISO pressure-velocity coupling scheme (Pressure-Implicit with Splitting of Operators) is also part of the SIMPLE family of algorithms and is based on a higher degree of approximation for the relation between the corrections for pressure and velocity [39]. The PISO algorithm takes a little more CPU time per solver iteration but it can dramatically decrease the number of iterations required for convergence, especially for transient problems. The PISO algorithm also allows Fluent to obtain solutions on highly skewed meshes in approximately the same number of iterations as required for more orthogonal meshes. Since all the simulation results described here were obtained on fairly regular meshes using time-independent calculations only the SIMPLE algorithm was employed in the calculations.

#### 4.2 Spatial Discretization

Fluent stores discrete values of the variables at the cell centres, however values of the variables are required at the cell faces for the convection terms in the equations and these must be interpolated from the cell centre values. This is accomplished using an upwind scheme and Fluent allows a

choice of several different upwind schemes: first-order upwind, second-order upwind, power law, and QUICK.

In the first-order upwind scheme quantities at cell faces are determined by assuming that the cell-centre values of any variable represent a cell-average value and hold throughout the entire cell. Hence the face quantities are identical to the cell quantities. The Power-Law scheme is an improvement which interpolates the face value of a variable by using the exact solution to a one-dimensional convection-diffusion equation [40]. When the flow is dominated by convection this implies that the face value of the variable is effectively equal to the cell value in the upwind direction. If the flow is weak and diffusion stronger then the Power-Law scheme amounts to a simple linear average of the value of the variable at the current cell location and the upstream cell. The Second-Order Upwind Scheme provides true second order accuracy by performing a Taylor series expansion of the cell-centred solution about the cell centroid. The QUICK scheme also allows calculation of a higher-order value of the convected variable at the cell face by using a weighted average of second-order upwind and central interpolation [41]. This scheme is particularly accurate on structured quadrilateral and hexahedral meshes where the flow is aligned with the grid direction. The Second-Order Upwind scheme was employed in all of the simulations described here.

## 5. Turbulence Models

Turbulent flows are characterized by velocity fields which fluctuate rapidly both in space and time. Since these fluctuations occur over several orders of magnitude it is computationally very expensive to construct a grid which directly simulates both the small scale and high frequency fluctuations for problems of practical engineering significance. Two methods can be used to eliminate the need to resolve these small scales and high frequencies: Reynolds Averaging and Filtering.

In the Reynolds Averaged approach all flow variables are divided into a mean component and a rapidly fluctuating component and then all equations are time averaged to remove the rapidly fluctuating components. For the continuity equation the new equation is identical to the original equation, except that the transported variables now represent the mean flow quantities. In the Navier-Stokes equation however new terms appear which involve mean values of products of rapidly varying quantities. These new terms are known as the Reynolds Stresses, and solution of the Reynolds Averaged Navier-Stokes (RANS) equation initially involves the construction of suitable models to represent these Reynolds Stresses. One approach to this problem is to treat the time averaged terms as additional viscous stresses produced by the turbulence in the flow. In the Boussinesq approach the Reynolds Stresses are assumed to have a form identical to the viscous stresses in the momentum equation, apart from a multiplicative term known as the turbulent viscosity,  $\mu_T$ . Note that this approach assumes that the Reynolds Stresses are isotropic, which is known to be untrue in many cases. The problem then reduces to finding an expression for  $\mu_T$ .

Fluent provides several turbulence models based on the Boussinesq approach: the Spalart-Allmaras model, the  $k-\varepsilon$  model, and the  $k-\omega$  model. The Spalart-Allmaras model is a relatively simple one-equation model which involves solving an additional model transport equation for  $\mu_T$ . Both the  $k-\varepsilon$  model and the  $k-\omega$  models are inherently more complicated and involve finding solutions to two additional model transport equations, one for the turbulent kinetic energy  $k$ , and one for the rate of dissipation of the turbulent kinetic energy  $\varepsilon$ , or in the case of the  $k-\omega$  model, an equation for  $\omega$  (where  $\omega$  is defined by  $\omega = \varepsilon / k$ ). The turbulent viscosity  $\mu_T$  is then calculated from an expression involving  $k$  and  $\varepsilon$  for the  $k-\varepsilon$  model, or  $k$  and  $\omega$  for the  $k-\omega$  model. There are in fact

three different versions of the  $k$ - $\varepsilon$  model in Fluent and two different versions of the  $k$ - $\omega$  model, and these will be discussed in more detail in the subsequent sections.

A turbulence model which avoids making the isotropic Boussinesq approximation is the Reynolds Stress Model (RSM). This is the most elaborate turbulence model that Fluent provides and finds a solution to the Reynolds-Averaged Navier-Stokes equation by solving additional transport equations for each of the individual Reynolds stresses, as well as an equation for the dissipation rate. This means that four additional transport equations are required in 2D flows and seven additional transport equations must be solved in 3D flows. Since the RSM accounts for the effects of streamline curvature, swirl, rotation, and rapid changes in strain rate in a more rigorous manner than one-equation (Spalart-Allmaras) and two-equation ( $k$ - $\varepsilon$  and  $k$ - $\omega$ ) models it has greater potential to give accurate predictions for complex flows. The accuracy of the RSM predictions is still limited, however, by the closure assumptions used to model various terms in the exact transport equations for the Reynolds stresses. For this reason the RSM does not always provide results which are superior to those of simpler models for all classes of flows. It is, of course, necessary to use the RSM when the flow features of interest are the result of anisotropy in the Reynolds stresses.

An alternative approach to Reynolds averaging is filtering. The idea behind this approach is to filter the time-dependent Navier-Stokes equation in either Fourier (wave-number) space or configuration (physical) space. This filtering process effectively filters out turbulent eddies whose scales are smaller than the filter width, which is usually taken to be the mesh size. As with Reynolds averaging however, the filtering process creates additional unknown terms which must be modelled in order to provide closure to the set of equations. This approach is known as Large Eddy Simulation (LES) because the fluctuations of the large scale eddies (those having a size comparable to the main geometry of the flow) are numerically resolved, rather than being averaged out as in the RANS approach. The attraction of LES is that, by modelling less of the turbulence (and solving more), the error introduced by the turbulence model will be reduced. Fluent provides two methods to model the subgrid-scale stresses resulting from the filtering operation: the Smagorinsky-Lilly model and the RNG (ReNormalization Group) subgrid-scale model. All LES simulations require a lengthy time-dependent run so that statistics of the mean flow quantities can be gathered. LES simulations also require a relatively fine grid, and so the computational cost of LES simulations can be quite prohibitive.

## 6. Computational Grid

The degree of resolution required of the computational grid depends to some extent on the choice of turbulence model to be used in the simulation. The  $k$ - $\varepsilon$  models, RSM, and LES models are primarily valid for turbulent core flows, i.e. for flow in the regions somewhat far from walls, while the Spalart-Allmaras and  $k$ - $\omega$  models were designed to be applied throughout the boundary layer, provided that the near-wall mesh resolution is sufficient. The  $k$ - $\varepsilon$  models can still be applied to wall bounded flows, however, by using the concept of wall functions. In this approach use is made of the universal behaviour of equilibrium boundary layer flows. It is well known that the near-wall region in an equilibrium boundary layer can be divided into several distinct regions [18]. Very close to the wall the flow is almost laminar and the molecular viscosity plays a dominant role in momentum transfer. This region is known as the “viscous sublayer”. At much greater distances from the wall, but still well within the boundary layer, molecular viscosity plays no part and the velocity profile is determined purely by the turbulent viscosity. This is known as the outer layer, or fully-turbulent layer. In between the viscous sublayer and the fully turbulent layer there is an

interim layer where the effects of molecular viscosity and turbulence are equally important. This is known as the buffer layer or blending region.

When standard wall functions are used the viscosity affected inner region (viscous sublayer and buffer layer) is not resolved. Instead, semi-empirical formulas are used to bridge the viscosity affected region between the wall and the fully turbulent region. The use of wall functions thus obviates the need to modify the turbulence model to account for the presence of the wall. In practice, this means that the centre of the cell closest to the wall must lie above a certain height. If  $y^+$  denotes the (scaled) co-ordinate direction normal to a solid wall and P denotes the centre point of the cell closest to the wall, then  $y^+_P$  should lie in the range  $30 < y^+_P < 100$ . If this criterion is satisfied then the boundary conditions can be satisfied at the point P by using the universal “log-law” for the mean velocity. Appropriate values for the other variables can also be derived at this location from the universal nature of the flow in this region.

With the above considerations in mind the first computational mesh consisted of a structured hexahedral mesh in which the cell centres closest to the wall were on average 2 mm above the flat plate and the surface of the wing. A total of 1.6 million hexahedral cells were used. This mesh was used to run simulations using the three different  $k-\varepsilon$  models available in Fluent: original  $k-\varepsilon$ , RNG  $k-\varepsilon$ , and renormalizeable  $k-\varepsilon$ , all using the standard wall functions. Because the resolution of the mesh was somewhat coarser than the resolution of the measurements used to characterize the input flat plate boundary layer none of these simulations used these measured values as input data. For each of these runs the  $y^+$  values varied between 40 and 60 over the surface of the plate and between 40 and 100 over the leading edge of the wing. Each of the simulations was able to accurately calculate the pressure distribution over the surface of the wing, but none of the simulations showed the presence of either a vortex or any reversed flow.

Since the first mesh proved to be too coarse a finer mesh was constructed so that the boundary layer profile measured upstream of the wing could be used as part of the inlet boundary conditions in the simulation. Because the aerofoil section had its major axis aligned with the free-stream flow a symmetry plane was created along the chord of the wing and only one half of the test section was meshed.

Devenport et al. [4] measured inflow conditions 1.31 m upstream of the leading edge of the wing ( $x/T = -18.24$ ). These consisted of velocity profiles measured at 29 locations along the Y axis between  $Y/T = 0.00354$  and  $Y/T = 0.87$  at  $Z = 0.0$ . The measured quantities were  $U/U_{ref}$  and mean values of  $u^2/U_{ref}^2$ ,  $w^2/U_{ref}^2$  and  $uw/U_{ref}^2$ . These measurements showed that the boundary layer had an initial thickness of approximately 2 cm and a structure very similar to that of a two-dimensional boundary layer under zero pressure gradient conditions. The height of the first data point above the flat plate was 0.2 mm and the average spacing between data points was 0.8 mm.

The computational grid extended from  $X = -1.3$  m to  $X = 1.3$  m in the X direction ( $X/T = -18.13$  to  $X/T = 18.13$ ),  $Y = 0.0$  to  $Y = 0.25$  m in the Y direction ( $Y/T = 3.49$ ) and  $Z = 0.0$  to  $Z = 0.5$  m in the Z direction ( $Z/T = 6.97$ ). The Y coordinate was divided into 100 intervals with the first grid point located at a height of approximately 0.1 mm above the flat plate. The size of successive intervals increased with a ratio of 1.04 so that the last interval had a height of approximately 1.0 cm. The surface of the wing along the X direction was meshed using 110 intervals. The first 20 intervals were of equal length (2.1 mm) and covered the elliptical part of the nose while the remaining 90 elements were of varying length (average length of 3.4 mm) and covered the NACA 0020 tail of the wing. The first 20 cm of the X coordinate upstream of the wing was meshed using elements of 2.15 mm length and similar gridding was used immediately downstream of the wing. At more distant locations grading was employed so that the length of the elements increased slowly to approximately 1 cm at the edges of the mesh. The mesh contained a total of 5 million hexahedral elements. The experimentally measured values of the velocity profile in the incoming boundary

layer flow (obtainable in digital form from [3]) were used for the velocity inlet boundary condition by constructing a Fluent Profile file which was read from the Velocity Inlet boundary panel.

## 7. Simulation Results

As well as the standard wall functions described in the previous section Fluent also provides both non-equilibrium wall functions and enhanced wall functions. The two key ingredients of the non-equilibrium wall functions are: (1) the log-law for the mean velocity is sensitised to pressure-gradient effects, (2) a two-layer zonal model is used to compute the budget of turbulent kinetic energy in the wall-neighbouring cells. In a standard wall function it is assumed that the cell-averaged rate of production of turbulent kinetic energy is identical to the cell-averaged dissipation rate of kinetic energy. The two-layer zonal model employed in the non-equilibrium wall functions relaxes this assumption by dividing each of the wall-neighbouring cells into a viscous sublayer and a fully turbulent layer and then computing the production and dissipation rates in each of the sublayers. Non-equilibrium wall functions therefore extend the applicability of the wall function approach by including the effects of pressure gradients and non-equilibrium kinetic energy production and can give improvements in the prediction of wall shear stress and heat transfer in flows where such effects occur.

Both standard wall functions and non-equilibrium wall functions become inappropriate when the flow contains either strong pressure gradient effects which result in boundary layer separation, or strongly skewed three-dimensional boundary layers. In this situation a near-wall modelling approach combined with adequate mesh resolution in the near-wall region must be used. Fluent provides an enhanced wall treatment for these situations and this approach can be used with all three  $k$ - $\varepsilon$  models as well as the RSM model. The enhanced wall treatment is a near-wall modelling method that combines a two-layer model with enhanced wall functions. In this approach the near-wall cells are divided into a viscosity-affected region and a fully-turbulent region. The demarcation between the two regions is determined by a wall distance based turbulent Reynolds number. In the fully turbulent region either the  $k$ - $\varepsilon$  model or the RSM model is employed, while in the viscosity-affected near wall region the one-equation model of Wolfstein [19] is used. In this method the momentum equations and the  $k$  equation is retained but the turbulent viscosity is computed from a simple expression involving  $k$  and an appropriate length scale. The exact details can be found in the Fluent 6.0 User's Guide Volume 2 [1]. When using the enhanced wall treatment with either the  $k$ - $\varepsilon$  models or the RSM model it is recommended that the  $y^+$  value at the wall adjacent cells should satisfy  $y^+ = 1$ , although higher  $y^+$  values are acceptable as long as  $y^+ < 5$ .

### 7.1 $k$ - $\varepsilon$ Model

The  $k$ - $\varepsilon$  model is the most widely used complete turbulence model and is incorporated in most commercial CFD codes. Fluent provides both the original  $k$ - $\varepsilon$  model as developed by Jones and Launder [20] and Launder and Sharma [21], as well as the RNG  $k$ - $\varepsilon$  model of Yakhot and Orszag [22] which is based on the application of the renormalization group method to the Navier-Stokes equation, and the realizable  $k$ - $\varepsilon$  model of Shih et al. [23] which is based on the application of certain constraints to the normal stresses to ensure that these remain positive at all times.

The standard  $k$ - $\varepsilon$  model is a semi-empirical model based on transport equations for the turbulent kinetic energy  $k$  and its dissipation rate  $\varepsilon$ . The transport equation for  $k$  was derived from the exact transport equation while the equation for  $\varepsilon$  was obtained using physical reasoning and cannot be justified on an exact mathematical basis. The turbulent viscosity is then specified by the equation



$\nu_T = C_\mu k^2/\varepsilon$ , where  $C_\mu = 0.09$  is one of five model constants. The RNG  $k$ - $\varepsilon$  model is derived from the instantaneous Navier-Stokes equation using the mathematical technique known as the renormalization group method. This results in a model with constants different from those in the standard  $k$ - $\varepsilon$  model and additional terms in the transport equation for  $\varepsilon$ .

The realizable  $k$ - $\varepsilon$  model of Shih et al. [23] was designed to remove two significant failings of previous  $k$ - $\varepsilon$  models, these being the tendency for the mean normal stresses (by definition these are positive quantities) to become negative in highly strained flows, and the rather empirical nature of the model transport equation for the dissipation rate  $\varepsilon$ . They achieved this by introducing a new eddy-viscosity formula in which  $C_\mu$  is no longer a constant but has a variable value which is a function of various flow parameters, and by introducing a new model equation for dissipation based on the dynamic equation for the mean-square vorticity fluctuation. Hence in the realizable  $k$ - $\varepsilon$  model the form of the  $k$  equation is identical to those in both the standard  $k$ - $\varepsilon$  model and the RNG  $k$ - $\varepsilon$  model, except for the model constants, while the form of the  $\varepsilon$  equation is quite different from those in the standard and RNG  $k$ - $\varepsilon$  models.

Since it is well known that the realizable  $k$ - $\varepsilon$  model consistently outperforms both the standard  $k$ - $\varepsilon$  model and the RNG  $k$ - $\varepsilon$  model in anything but the simplest flow geometries [18], only the realizable  $k$ - $\varepsilon$  model has been used for the simulation results described here. This version was run on the grid described in the previous section using enhanced wall functions and the second order Upwind scheme for the solution of the momentum,  $k$  and  $\varepsilon$  equations. The pressure-velocity coupling used the SIMPLE scheme and the boundaries simulating the wind tunnel walls were defined as solid walls with specified zero shear stress. The  $y^+$  values along the centre line of the wind tunnel floor upstream of the wing satisfied  $y^+ = 3$  while downstream of the wing they satisfied  $y^+ = 4$  and away from the centre line approached  $y^+ = 6$ . Along the wing surface the  $y^+$  values varied from approximately 8 on the nose to 4 along the trailing edge. These values are reasonably consistent with those specified above and described in the Fluent 6.0 User's Guide Volume 2 [1]. The model constants used for this particular implementation are:  $C_{1\varepsilon} = 1.44$ ,  $C_2 = 1.9$ ,  $\sigma_k = 1.0$  and  $\sigma_\varepsilon = 1.2$ .

Figures 3 and 4 show the pressure coefficient around the wing surface, from the leading edge to the trailing edge, at two horizontal sections, i.e.  $Y/T = 0.133$  and  $Y/T = 1.726$ . An interesting feature of these plots is that agreement with experiment is better closer to the wall (Fig.3) than away from it (Fig. 4). Apsley and Leschziner [10] found exactly the same behaviour in their simulations and also showed that this result was not due to grid dependent solutions. They concluded that the most likely cause of the difference between the simulated and experimental peak pressure shown in Fig. 4 was a discrepancy between the prescribed and experimental flow conditions at the upper boundary of the computational domain. In the real flow there was a gap between the top of the wing and the upper tunnel wall while in the computation (both in Apsley and Leschziner's and those reported here) the wing extended to touch the upper surface of the wind tunnel. In our view this explanation is unlikely as the pressure profile at  $Y/T = 1.46$  is identical to the value at  $Y/T = 1.726$ , and the value at  $Y/T = 0.400$  also shows a peak at this point.

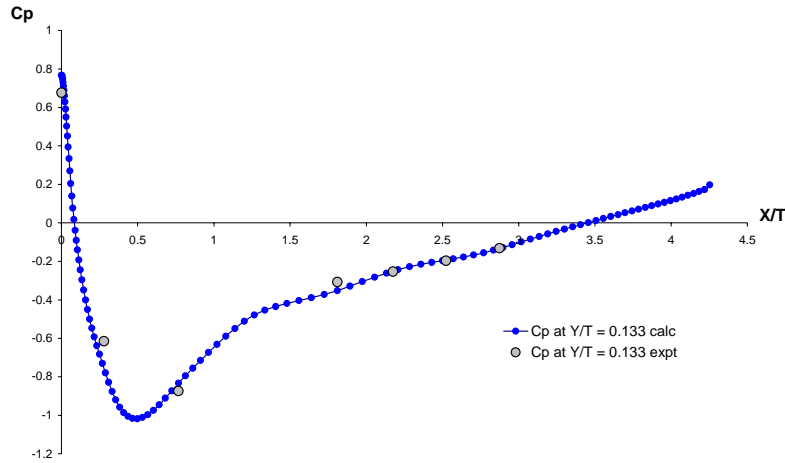


Figure 3. Pressure coefficient along the wing surface at a height of  $Y/T = 0.133$  for the Realizable  $k-\epsilon$  model.

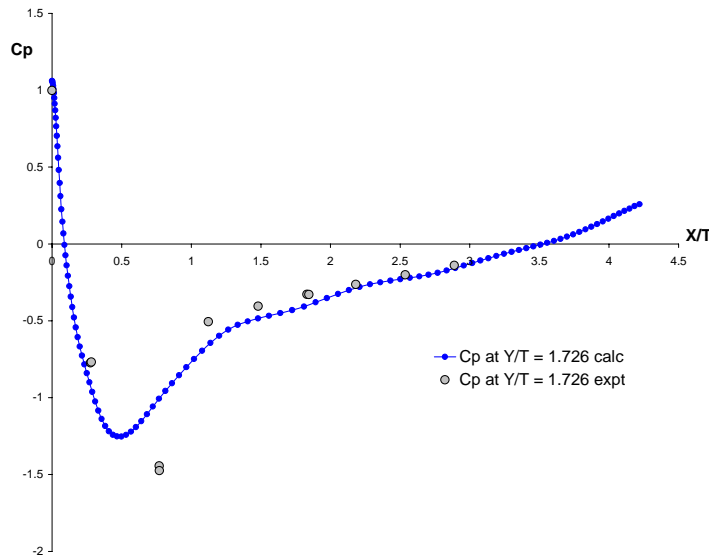


Figure 4. Pressure coefficient along the wing surface at a height of  $Y/T = 1.726$  for the Realizable  $k-\epsilon$  model.

Figures 5 through 9 show a comparison between the simulated and experimental values of  $U/U_{\text{ref}}$  versus  $Y/T$  at selected  $X/T$  values. For  $X/T$  values removed from the centre of the vortex, i.e. those in the range between  $-0.860$  and  $-0.404$ , there is fairly good agreement between the simulated and experimental values. Even at the station closest to the nose of the wing, at  $X/T = -0.050$ , there is still quite good agreement between the experimental values and the simulated values over most of the range of  $Y/T$ . At  $X/T = -0.103$  there is still reasonable agreement, but from  $X/T = -0.154$  up to  $X/T = -0.351$  there is significant disagreement between simulation and experiment. The Realizable  $k-\epsilon$  model essentially underestimates the strength of the reverse flow in the vortex region, and this is the same result as noted by Apsley and Leschziner [10] when using the standard  $k-\epsilon$  model.

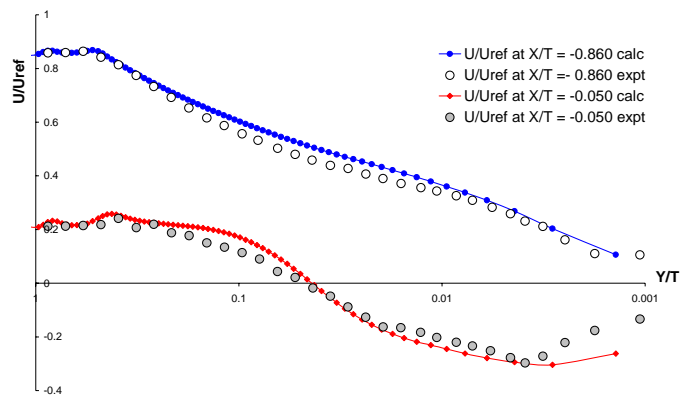


Figure 5. Comparison of simulated and experimental values of  $U/U_{ref}$  versus  $Y/T$  at  $X/T = -0.050$  and  $X/T = -0.860$  for the Realizable  $k-\epsilon$  model.

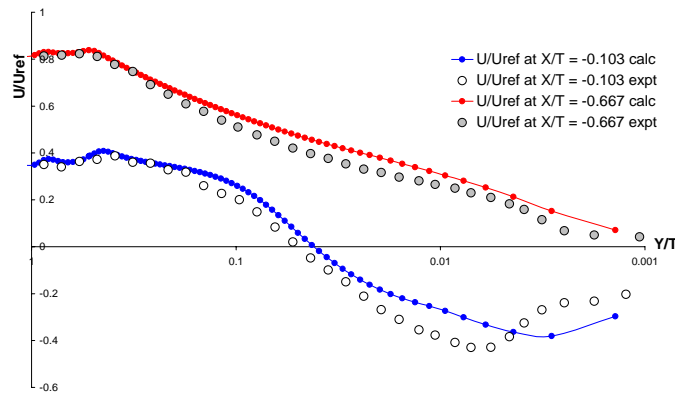


Figure 6. Comparison of simulated and experimental values of  $U/U_{ref}$  versus  $Y/T$  at  $X/T = -0.103$  and  $X/T = -0.667$  for the Realizable  $k-\epsilon$  model.

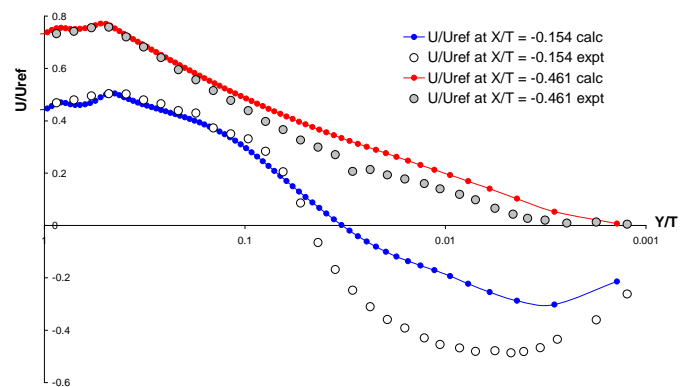


Figure 7. Comparison of simulated and experimental values of  $U/U_{ref}$  versus  $Y/T$  at  $X/T = -0.154$  and  $X/T = -0.461$  for the Realizable  $k-\epsilon$  model.

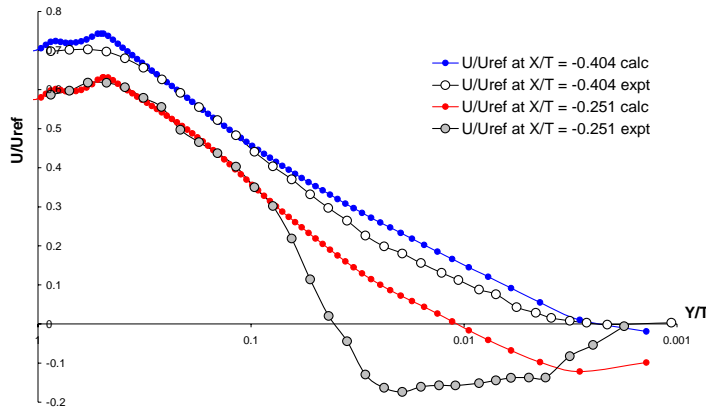


Figure 8. Comparison of simulated and experimental values of  $U/U_{ref}$  versus  $Y/T$  at  $X/T = -0.251$  and  $X/T = -0.404$  for the Realizable  $k-\varepsilon$  model.

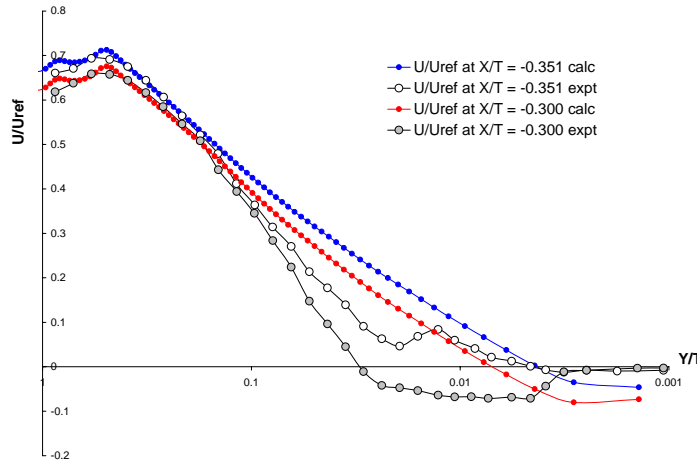


Figure 9. Comparison of simulated and experimental values of  $U/U_{ref}$  versus  $Y/T$  at  $X/T = -0.300$  and  $X/T = -0.351$  for the Realizable  $k-\varepsilon$  model.

Figures 10 and 11 show the experimental and calculated values for  $V/U_{ref}$  versus  $Y/T$  at all the  $X/T$  stations. The simulated results clearly show the same trend as the experimental values, with those  $X/T$  locations closest to the wing displaying the largest negative values of velocity. Noticeably absent however are the positive components of the velocity for those stations closest to the centre of the vortex, those at  $X/T = -0.204$  and  $X/T = -0.251$  for example, where the experimental results show positive velocity components above  $Y/T = 0.1$ , while the simulated results are unable to capture this behaviour to any extent. A more detailed comparison between the experimental and simulated values is shown in Figures 12 and 13. These show that at some of the  $X/T$  stations there is quite reasonable agreement. For example, at  $X/T = -0.050, -0.204, -0.251, -0.300, -0.404$ , and  $-0.461$  the simulated curves follow the experimental curves quite closely, while at  $X/T = -0.103$  and  $-0.154$  there is considerable disagreement.

Figure 14 shows a comparison between the simulated and experimental values of the turbulent kinetic energy as a function of  $Y/T$  for selected  $X/T$  values. Experimentally the peak value of the turbulent kinetic energy occurs close to the centre of the vortex at  $X/T = -0.351$  and  $Y/T = 0.05$ ,

with the values either side of the vortex, at  $X/T = -0.050$  and  $X/T = -0.860$ , being considerably lower than those near the centre. The simulated results display quite a different trend. The kinetic energy increases continuously as the distance to the wing decreases, and the maximum value occurs not at the vortex centre but rather at the closest point to the wing surface. This behaviour also occurs in the simulations of Apsley and Leschziner [10], Parneix et al. [11], and Rodi et al. [12], and is a known fault with all  $k-\varepsilon$  models.

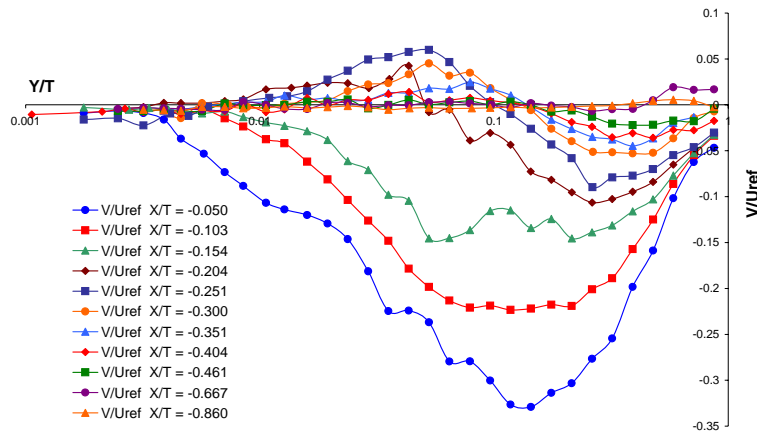


Figure 10. Experimental values of  $V/U_{ref}$  versus  $Y/T$  at all  $X/T$  stations.

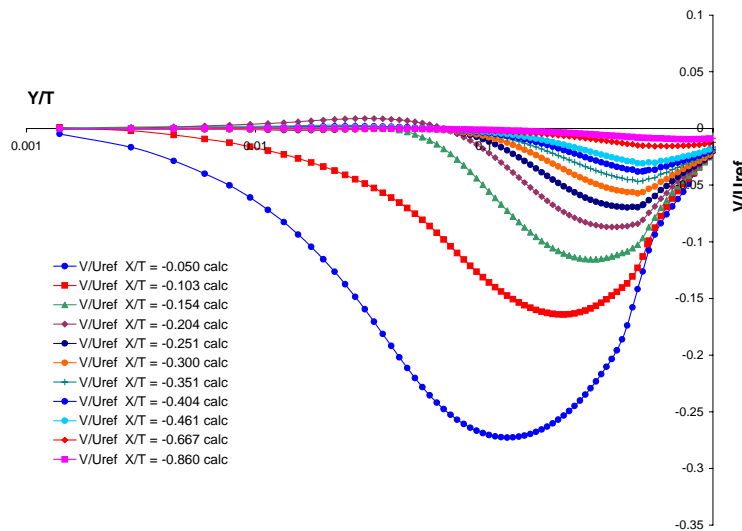


Figure 11. Simulated values of  $V/U_{ref}$  versus  $Y/T$  at all  $X/T$  stations for the Realizable  $k-\varepsilon$  model.

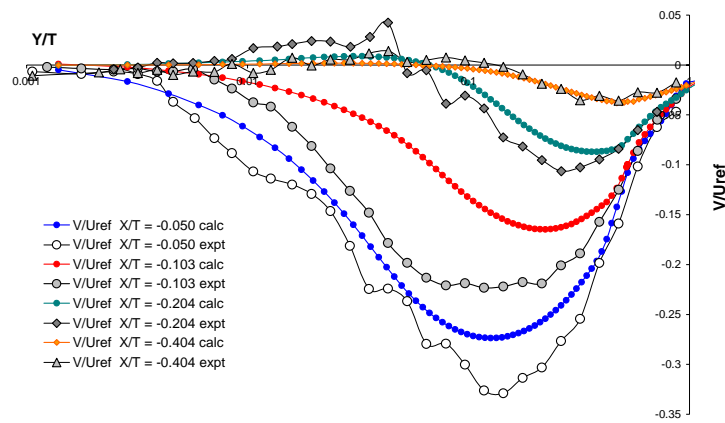


Figure 12. Comparison of simulated and experimental values of  $V/U_{ref}$  versus  $Y/T$  at selected  $X/T$  values for the Realizable  $k-\epsilon$  model.

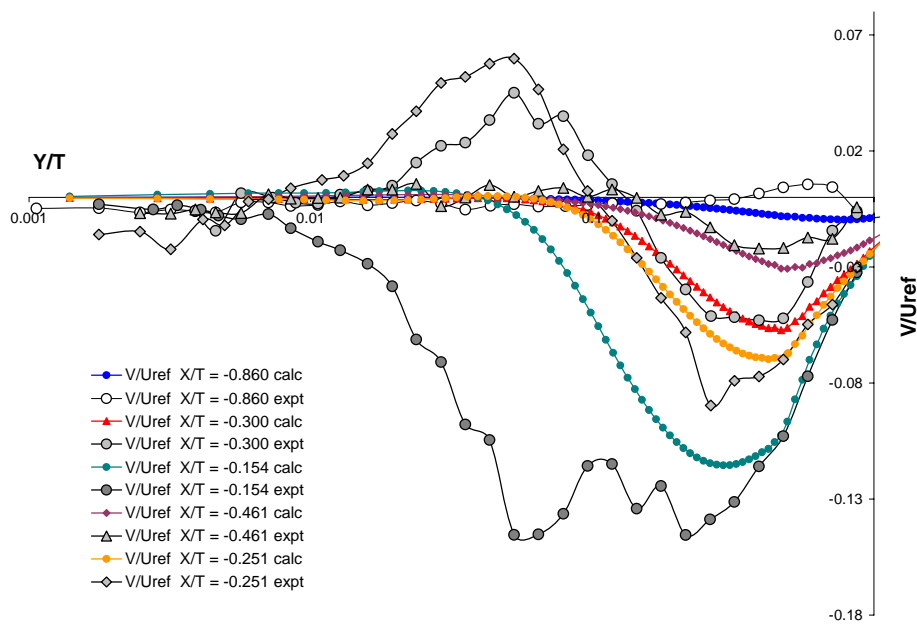


Figure 13. Comparison of simulated and experimental values of  $V/U_{ref}$  versus  $Y/T$  at selected  $X/T$  values for the Realizable  $k-\epsilon$  model.

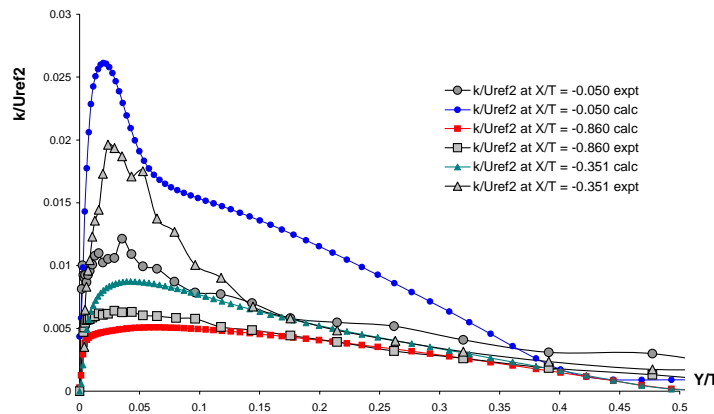


Figure 14. Comparison of simulated and experimental values of  $k/U_{ref}^2$  versus  $Y/T$  at selected  $X/T$  values for the Realizable  $k-\epsilon$  model.

## 7.2 Reynolds Stress Model

This is the most elaborate RANS turbulence model provided in Fluent and since it avoids making the isotropic Boussinesq approximation by solving additional transport equations for each of the individual Reynolds stresses it is expected to provide superior results to any of the other models. The model constants used for this particular implementation are:  $C_1 = 3.4$ ,  $C_1^* = 1.8$ ,  $C_2 = 4.2$ ,  $C_3 = 0.8$ ,  $C_3^* = 1.3$ ,  $C_4 = 1.25$  and  $C_5 = 0.4$ .

Figures 15 through 19 show a comparison between the simulated and experimental values of  $U/U_{ref}$  versus  $Y/T$  at selected  $X/T$  values. The level of agreement between simulation and experiment at  $X/T$  locations  $-0.050$ ,  $-0.103$ ,  $-0.154$ ,  $-0.461$ ,  $-0.667$  and  $-0.860$  is very similar to that found for the Realizable  $k-\epsilon$  model. At locations close to the vortex however, for  $X/T$  values of  $-0.251$ ,  $-0.300$  and  $-0.351$ , the RSM model provides considerably better agreement than the Realizable  $k-\epsilon$  model. The only location at which the Realizable  $k-\epsilon$  model provides better agreement than the RSM model occurs at  $X/T = -0.404$ .

Figures 20 through 22 compare the experimental and calculated values for  $V/U_{ref}$  versus  $Y/T$  at all the  $X/T$  stations. Comparison with Figures 12 and 13 show that the RSM model provides significant improvement over results obtained using the Realizable  $k-\epsilon$  model for all of the  $V/U_{ref}$  plots. There is now much better agreement between the simulated and experimental values at  $X/T = -0.103$  and  $-0.154$ , while at locations close to the centre of the vortex, such as  $X/T = -0.251$  and  $X/T = -0.300$  for example, the RSM model captures the positive components of the velocity which occur above  $Y/T = 0.1$ .

Figure 23 shows a comparison between the simulated and experimental values of the turbulent kinetic energy as a function of  $Y/T$  for selected  $X/T$  values. The results are similar to those shown in Figure 14 for the Realizable  $k-\epsilon$  model in that the peak in the kinetic energy again occurs at the location closest to the wall, but at least the level of agreement between the simulated and experimental value at  $X/T = -0.351$  is considerably improved. In summary, the RSM model seems to provide better agreement with experiment for the mean velocity components than does the Realizable  $k-\epsilon$  model, but the turbulent kinetic energy is still poorly predicted.

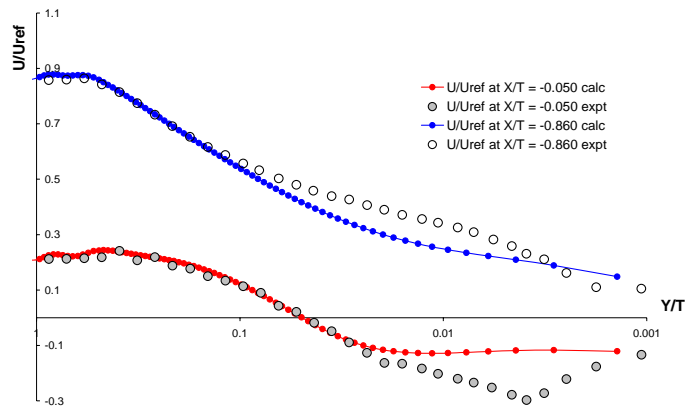


Figure 15. Comparison of simulated and experimental values of  $U/U_{ref}$  versus  $Y/T$  at  $X/T = -0.050$  and  $X/T = -0.860$  for the RSM model.

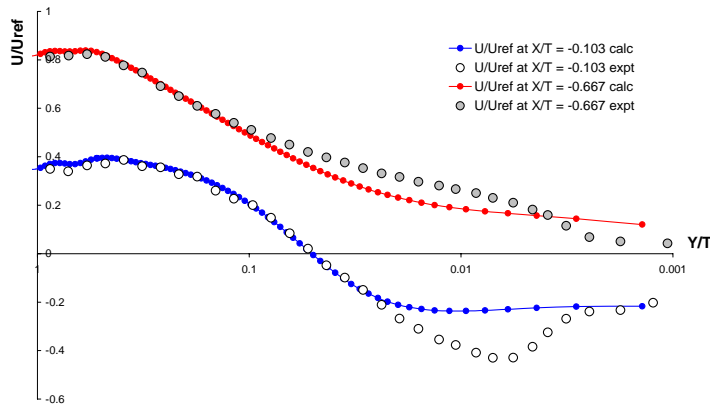


Figure 16. Comparison of simulated and experimental values of  $U/U_{ref}$  versus  $Y/T$  at  $X/T = -0.103$  and  $X/T = -0.667$  for the RSM model.

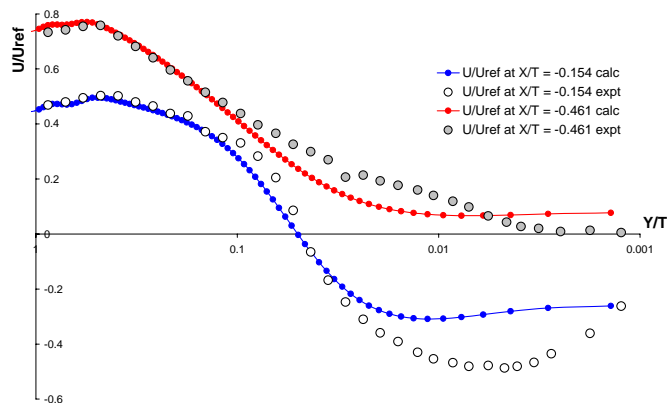


Figure 17. Comparison of simulated and experimental values of  $U/U_{ref}$  versus  $Y/T$  at  $X/T = -0.154$  and  $X/T = -0.461$  for the RSM model.



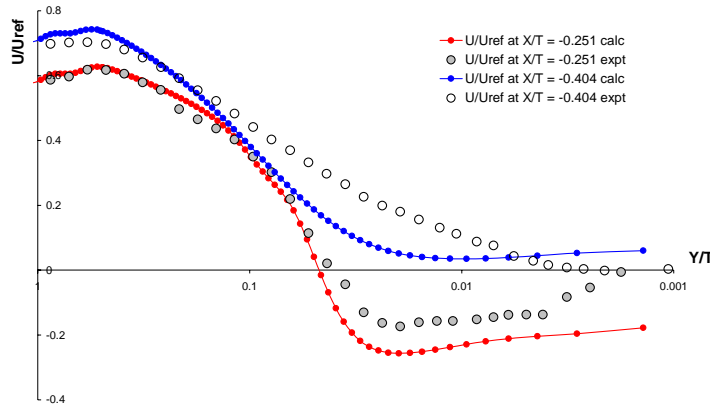


Figure 18. Comparison of simulated and experimental values of  $U/U_{ref}$  versus  $Y/T$  at  $X/T = -0.251$  and  $X/T = -0.404$  for the RSM model.

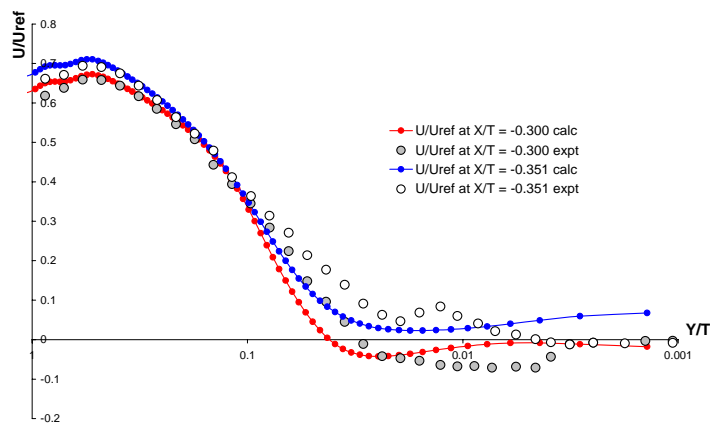


Figure 19. Comparison of simulated and experimental values of  $U/U_{ref}$  versus  $Y/T$  at  $X/T = -0.300$  and  $X/T = -0.351$  for the RSM model.

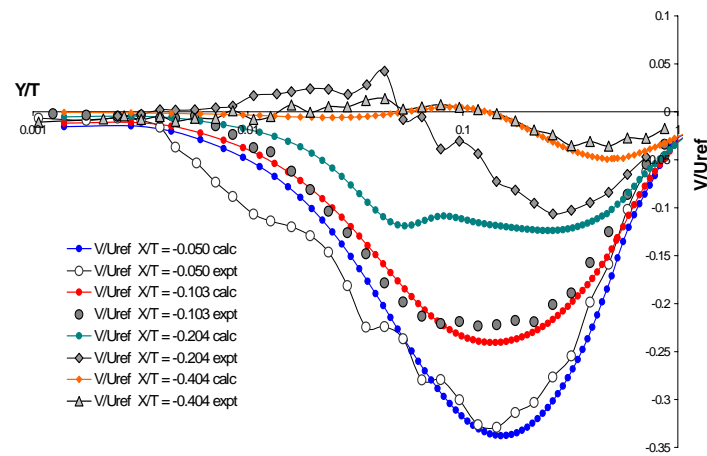


Figure 20. Comparison of simulated and experimental values of  $V/U_{ref}$  versus  $Y/T$  at selected  $X/T$  values for the RSM model

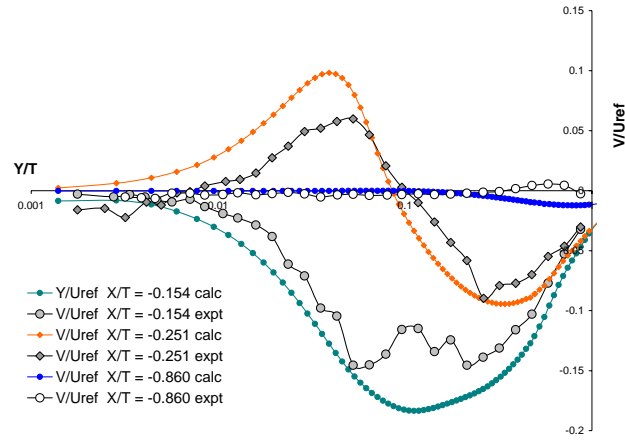


Figure 21. Comparison of simulated and experimental values of  $V/U_{ref}$  versus  $Y/T$  at selected  $X/T$  values for the RSM model

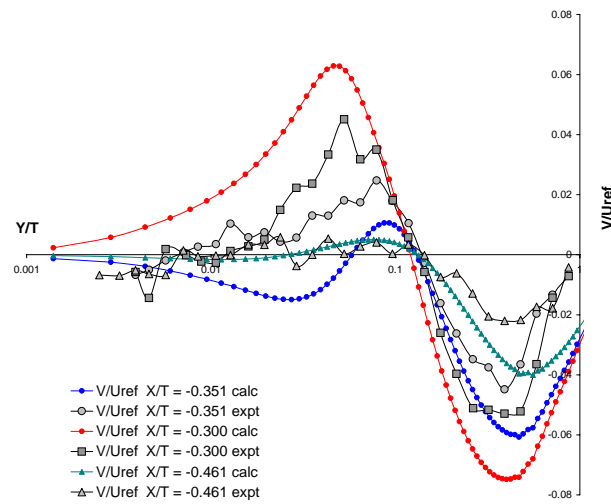


Figure 22. Comparison of simulated and experimental values of  $V/U_{ref}$  versus  $Y/T$  at selected  $X/T$  values for the RSM model

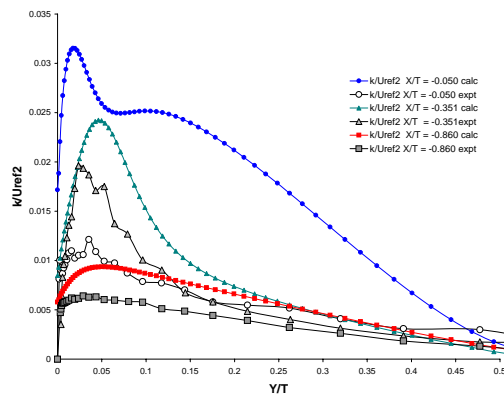


Figure 23. Comparison of simulated and experimental values of  $k/U_{ref}^2$  versus  $Y/T$  at selected  $X/T$  values for the RSM.

### 7.3 V2F Model

This model was developed by Durbin in a number of publications [24-27] during the period 1991-1995 and is available in Fluent by payment of an additional licence fee. Conceptually the model lies somewhere between the simplicity of an isotropic  $k$ - $\varepsilon$  model and the full anisotropy provided by a Reynolds Stress model. It arose out of a desire to eliminate the need to use wall functions or the two-layer approach to specify how turbulence varies near a wall. It was developed from a simplified Reynolds Stress model and successfully includes the anisotropy of near-wall turbulence while continuing to use an eddy viscosity assumption. The model is valid throughout the whole flow domain and automatically becomes a near-wall model close to solid surfaces. It uses the standard  $k$ - $\varepsilon$  equations as well as an additional transport equation for the mean value of  $v^2$ , where  $v$  represents the component of the fluctuating velocity normal to the time-averaged streamline, and an elliptic relaxation equation for the function  $f$ , which can be taken to represent the redistribution of turbulent intensity from the streamwise component of the flow. The elliptic equation models pressure-velocity correlations and accounts for the non-local effect of blocking by the wall, ensuring that the velocity component normal to the wall is inviscidly brought to zero at the wall. The turbulent viscosity is then given by the expression  $\nu_T = C_\mu \overline{v^2} k / \varepsilon$ , where  $C_\mu$  has the value 0.2. The model has a built-in realizability limiter (Durbin [28]) and does not require any damping or wall functions to correctly capture near-wall turbulence.

Figures 24 through 28 show a comparison between the simulated and experimental values of  $U/U_{ref}$  versus  $Y/T$  at selected  $X/T$  values. The level of agreement between simulation and experiment is certainly better than that shown by the Realizable  $k$ - $\varepsilon$  model and comparable with that shown by the full RSM model. In fact at  $X/T = -0.050, -0.103, -0.154$  and  $-0.404$  there is better agreement between the simulated and experimental results, with the only location showing slightly worse agreement being at  $X/T = -0.251$ .

Figures 29 through 31 compare the simulated and experimental values for  $V/U_{ref}$  versus  $Y/T$  at all the  $X/T$  stations. Comparison with Figures 12 and 13 for the Realizable  $k$ - $\varepsilon$  model and Figures 20 through 22 for the RSM model show that the V2F model provides far better agreement with the experimental values than the Realizable  $k$ - $\varepsilon$  model and a similar degree of agreement as the RSM model. At  $X/T = -0.050$  and  $-0.103$  for example the RSM model provides better agreement with experiment than the V2F model, while at  $X/T = -0.204, -0.251, -0.300$  and  $-0.351$  the V2F model provides better agreement than the RSM model. These figures show that the V2F model, similar to the RSM model, is capable of capturing the positive components of the velocity which occur above  $Y/T = 0.1$  in the area of the vortex centre.

Figure 32 shows the simulated and experimental values of the turbulent kinetic energy as a function of  $Y/T$  for the same  $X/T$  locations shown in Figure 14 for the Realizable  $k$ - $\varepsilon$  model and Figure 23 for the RSM model. The results here are an improvement on those calculated using either the Realizable  $k$ - $\varepsilon$  model or the RSM model close to the wall, but agreement is worse near the centre of the vortex. The V2F model however still shows the peak turbulent kinetic energy close to the wall, rather than at the vortex centre.

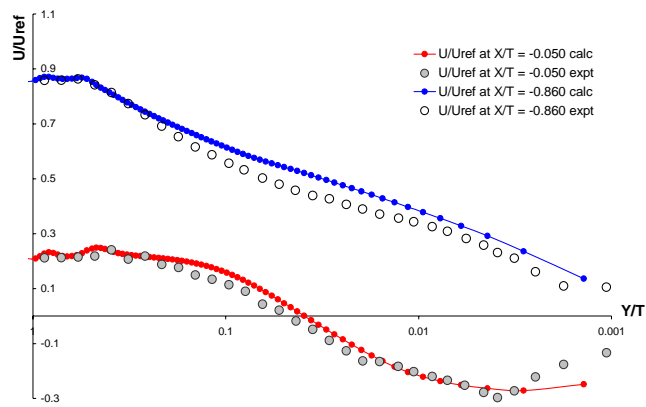


Figure 24. Comparison of simulated and experimental values of  $U/U_{ref}$  versus  $Y/T$  at  $X/T = -0.050$  and  $X/T = -0.860$  for the V2F model.

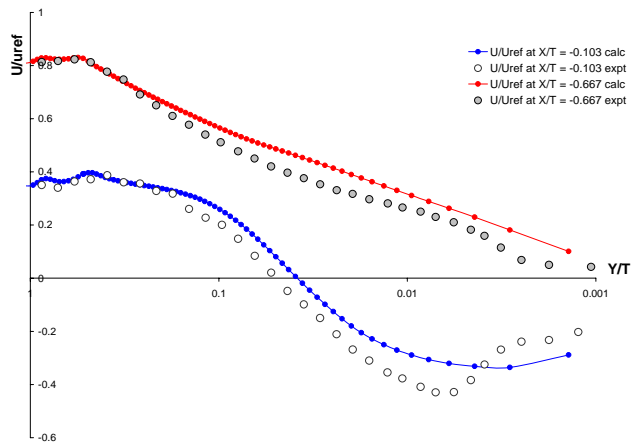


Figure 25. Comparison of simulated and experimental values of  $U/U_{ref}$  versus  $Y/T$  at  $X/T = -0.103$  and  $X/T = -0.667$  for the V2F model.

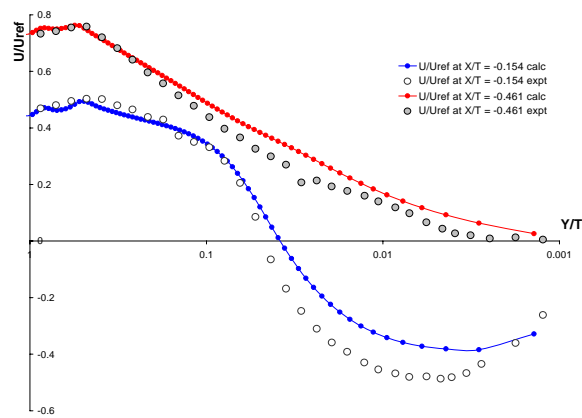


Figure 26. Comparison of simulated and experimental values of  $U/U_{ref}$  versus  $Y/T$  at  $X/T = -0.154$  and  $X/T = -0.461$  for the V2F model.

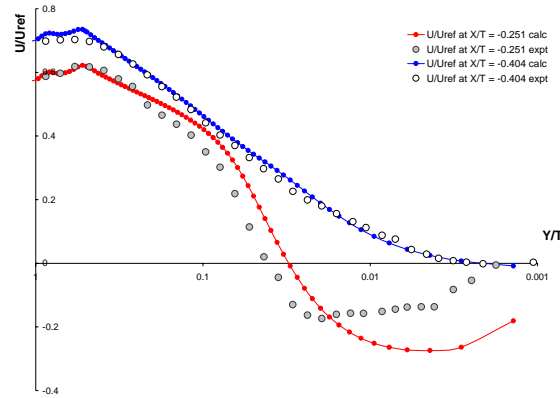


Figure 27. Comparison of simulated and experimental values of  $U/U_{ref}$  versus  $Y/T$  at  $X/T = -0.251$  and  $X/T = -0.404$  for the V2F model.

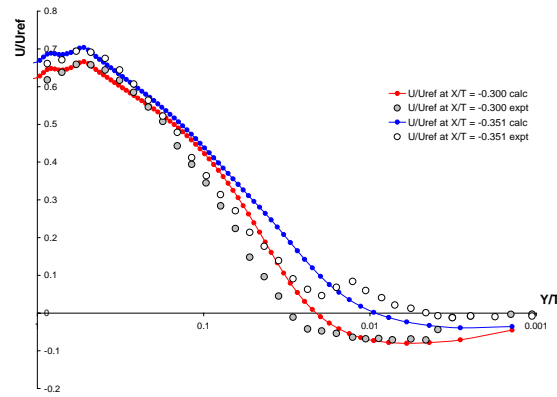


Figure 28. Comparison of simulated and experimental values of  $U/U_{ref}$  versus  $Y/T$  at  $X/T = -0.300$  and  $X/T = -0.351$  for the V2F model.

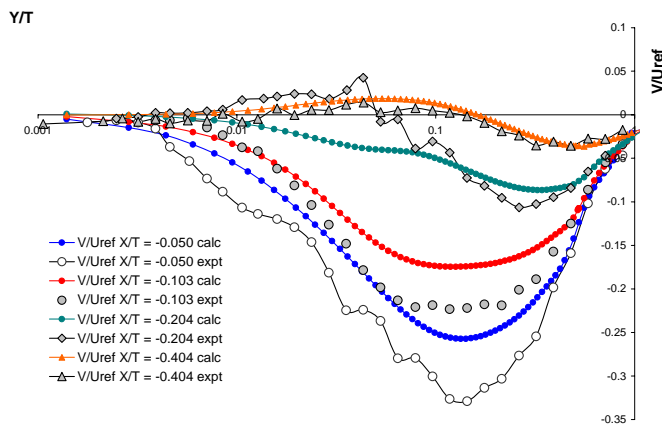


Figure 29. Comparison of simulated and experimental values of  $V/U_{ref}$  versus  $Y/T$  at selected  $X/T$  values for the V2F model.

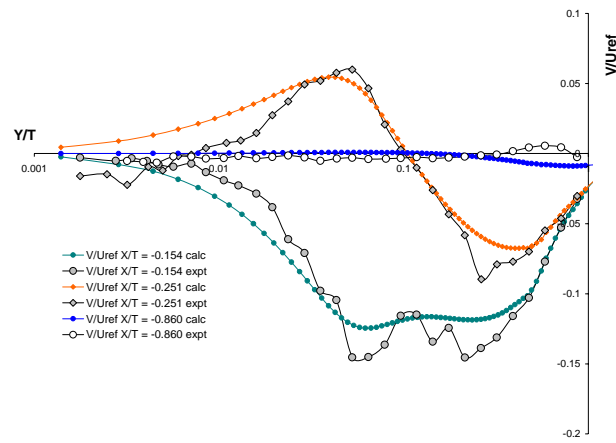


Figure 30. Comparison of simulated and experimental values of  $V/U_{ref}$  versus  $Y/T$  at selected  $X/T$  values for the V2F model.

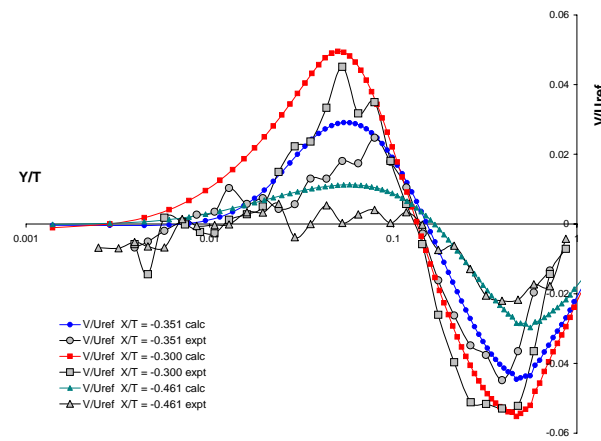


Figure 31. Comparison of simulated and experimental values of  $V/U_{ref}$  versus  $Y/T$  at selected  $X/T$  values for the V2F model.

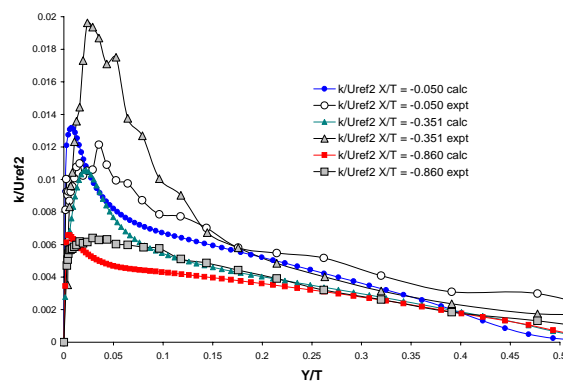


Figure 32. Comparison of simulated and experimental values of  $k/U_{ref}^2$  versus  $Y/T$  at selected  $X/T$  values for the V2F model.

## 7.4 Spalart-Allmaras Model

This is the simplest turbulence model provided in Fluent. It solves the RANS equations for the mean velocity components and pressure and uses the Boussinesq hypothesis to relate the Reynolds stresses to the mean velocity gradients. The turbulent viscosity is then found from the solution of one additional transport equation. The derivation of this equation is explained in detail in the original paper by Spalart and Allmaras [29]. Rather than being derived in a more or less fundamental way from moments of the Navier-Stokes equation, as are the equations for  $k$  and  $\varepsilon$  in the  $k$ - $\varepsilon$  model, the transport equation for the turbulent viscosity is simply postulated, based on a combination of empiricism, dimensional analysis, Galilean invariance, and selective dependence on the molecular viscosity. In its original formulation it contains production, destruction and diffusion terms, with both the production and destruction terms being a function of the distance to the wall, and the production term also being a function of the magnitude of the vorticity. The model was designed specifically for aerospace applications involving wall-bounded flows and has been shown to give good results for boundary layers subjected to adverse pressure gradients.

Fluent contains both the original version of the model as well as a modified form which takes into account the effect of mean strain on the turbulence production. This modification combines measures of both rotation and strain tensors in the definition of the production term. Including both the rotation and strain tensors reduces the production of eddy viscosity and consequently reduces the eddy viscosity itself in regions where the measure of the vorticity exceeds that of the strain rate. This is typically found in vortical flows near the core of a vortex subjected to pure rotation where turbulence is known to be suppressed. This is the opposite of the case under study here, where the turbulence production in the core of the vortex is considerably enhanced, and so only the original version of the model has been used in this report.

The original Spalart-Allmaras model was effectively a low Reynolds number model and required fine resolution in the viscosity affected region of the boundary layer. In Fluent, however, the model has been implemented to use wall functions when the mesh resolution is not sufficiently fine. Guidelines for the use of this model, as described in the Fluent 6.1 Tutorial Guide Number 3 [30], indicate that the  $y^+$  value of the wall adjacent cells should be either very small (on the order of  $y^+ = 1$ ), or approximately 30 or greater. Paciorri et al. [31] used the Spalart-Allmaras model to simulate flow around a hollow-cylinder flare problem and found excellent agreement with the experimental data provided that the wall  $y^+$  value did not exceed a value of 2. On a more coarse mesh, where the  $y^+$  value exceeded 6, the agreement with experiment was severely degraded. Since the  $y^+$  values on the present grid were of the order of 5 and 6, a new mesh was constructed with finer resolution in the areas close to the wall. The height of the first layer of cells above the solid surfaces was changed from 0.1mm to approximately 0.03 mm and stronger growth ratios were used so that the cell sizes at the edges of the mesh were approximately 2 cm. The resulting  $y^+$  values around the base of the wing varied between 0.5 to 1.5, while over the leading edge of the wing the maximum  $y^+$  value was approximately 2. The model constants used for this particular implementation are:  $C_{b1} = 0.1335$ ,  $C_{b2} = 0.622$ ,  $\sigma_v = 2/3$ ,  $C_{v1} = 7.1$ ,  $C_{w1} = C_{b1}/\kappa_2 + (1+C_{b2})/\sigma_v$ ,  $C_{w2} = 0.3$ ,  $C_{w3} = 2.0$  and  $\kappa = 0.4187$ .

Figures 33 through 37 show a comparison between the simulated and experimental values of  $U/U_{ref}$  versus  $Y/T$  at selected  $X/T$  values. The level of agreement between simulation and experiment is again noticeably better than that shown by the Realizable  $k$ - $\varepsilon$  model and comparable with that shown by the full RSM model or the V2F model. At  $X/T = -0.050, -0.103, -0.154, -0.461, -0.667$  and  $-0.860$  all the models show very similar levels of agreement, although at  $X/T = -0.251, -$

0.404 and -0.461 both the V2F model and the Spalart-Allmaras model show better agreement with experiment, and the Spalart-Allmaras results are remarkably similar to those of the V2F model. At  $X/T = -0.300$  and  $-0.351$  however the Spalart-Allmaras results are inferior to those of either the RSM or V2F models, although they are still better than those calculated by the Realizable  $k-\varepsilon$  model.

Figures 38 through 40 compare the simulated and experimental values for  $V/U_{ref}$  versus  $Y/T$  at all the  $X/T$  stations. These demonstrate again that the level of agreement between simulation and experiment is noticeably better than that shown by the Realizable  $k-\varepsilon$  model and comparable with that shown by the full RSM model or the V2F model. Only at  $X/T = -0.251$  does the Spalart-Allmaras model fail to predict the positive velocity component which occurs close to the wall in the area of the vortex centre. Note that since the Spalart-Allmaras model solves a transport equation for the turbulent viscosity rather than the turbulent kinetic energy we are unable to make a comparison between simulated and experimental values of the turbulent kinetic energy as a function of  $Y/T$  at the  $X/T$  locations.

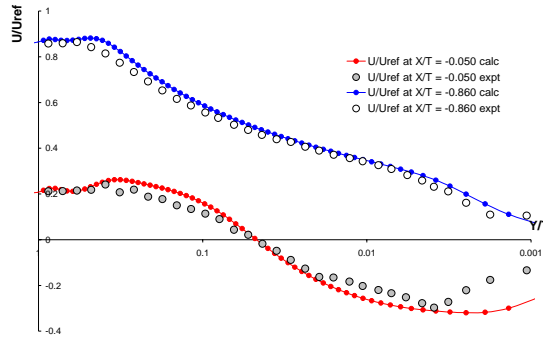


Figure 33. Comparison of simulated and experimental values of  $U/U_{ref}$  versus  $Y/T$  at  $X/T = -0.050$  and  $X/T = -0.860$  for the Spalart-Allmaras model.

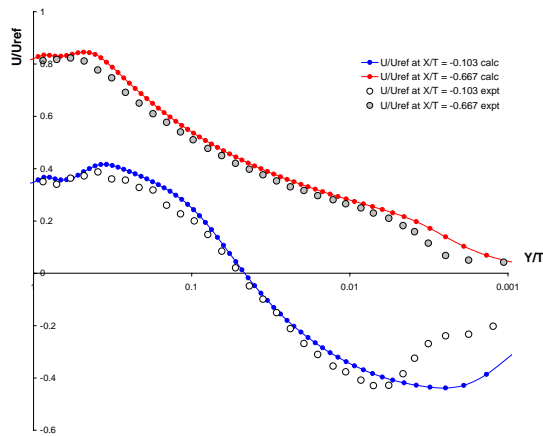


Figure 34. Comparison of simulated and experimental values of  $U/U_{ref}$  versus  $Y/T$  at  $X/T = -0.103$  and  $X/T = -0.667$  for the Spalart-Allmaras model.



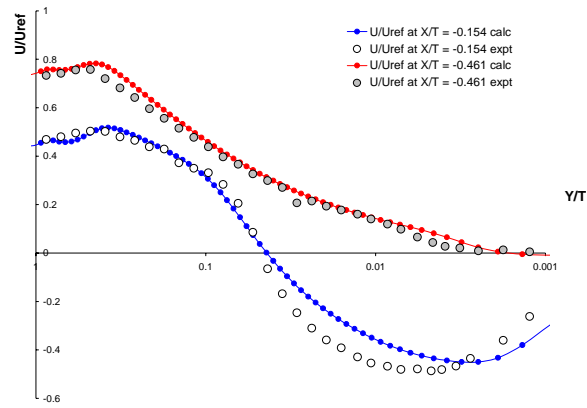


Figure 35. Comparison of simulated and experimental values of  $U/U_{ref}$  versus  $Y/T$  at  $X/T = -0.154$  and  $X/T = -0.461$  for the Spalart-Allmaras model.

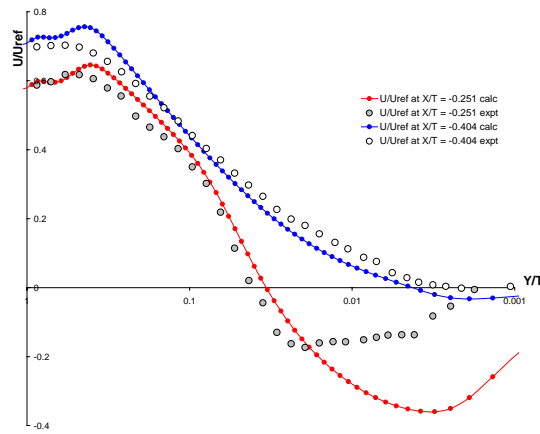


Figure 36. Comparison of simulated and experimental values of  $U/U_{ref}$  versus  $Y/T$  at  $X/T = -0.251$  and  $X/T = -0.404$  for the Spalart-Allmaras model.

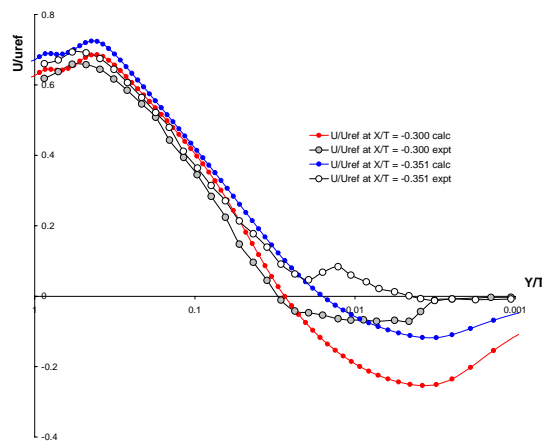


Figure 37. Comparison of simulated and experimental values of  $U/U_{ref}$  versus  $Y/T$  at  $X/T = -0.300$  and  $X/T = -0.351$  for the Spalart-Allmaras model.

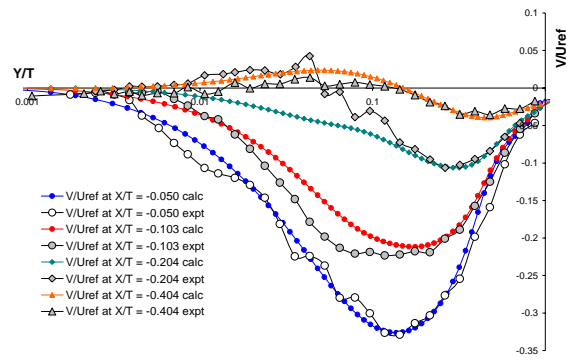


Figure 38. Comparison of simulated and experimental values of  $V/U_{ref}$  versus  $Y/T$  at selected  $X/T$  values for the Spalart-Allmaras model.

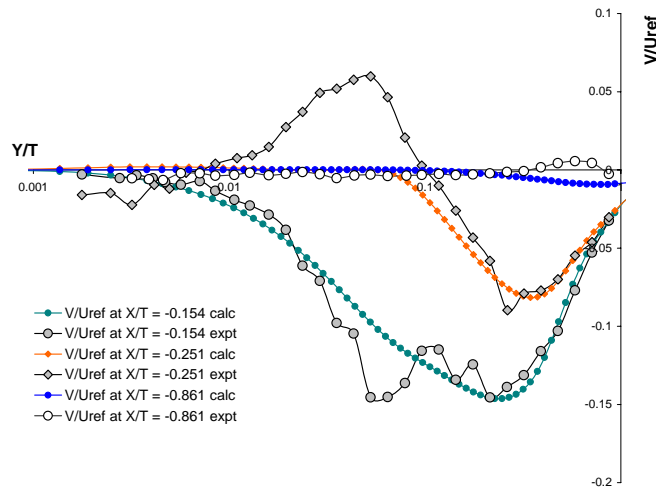


Figure 39. Comparison of simulated and experimental values of  $V/U_{ref}$  versus  $Y/T$  at selected  $X/T$  values for the Spalart-Allmaras model.

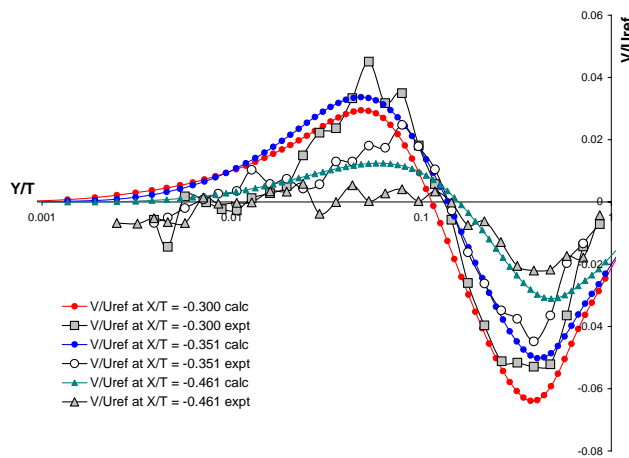


Figure 40. Comparison of simulated and experimental values of  $V/U_{ref}$  versus  $Y/T$  at selected  $X/T$  values for the Spalart-Allmaras model.

## 7.5 $k$ - $\omega$ Model

The  $k$ - $\omega$  model is the second most widely used two equation model. It was developed by Wilcox in 1988 [32], although an improved version appeared in the book by Wilcox in 1998 [33]. In this model the expression for the turbulent viscosity and the equation for the turbulent kinetic energy are the same as those used in the  $k$ - $\varepsilon$  model. The difference between the two models lies in the second equation, which Wilcox writes as an equation for the variable  $\omega$ , which is the dissipation per unit turbulence kinetic energy and is defined simply as  $\omega \equiv \varepsilon / k$ . Wilcox has shown that, for boundary layer flows, the  $k$ - $\omega$  model is superior to the  $k$ - $\varepsilon$  model both in its treatment of the viscous near wall region and in its accounting for the effects of streamwise pressure gradients. The original model had problems near non-turbulent free stream boundaries because a non-zero (non-physical) boundary condition is required for  $\omega$  and the calculated flow was found to be sensitive to the value specified. The modified  $k$ - $\omega$  model described by Wilcox in 1998 [33] has removed this problem.

A different version of the  $k$ - $\omega$  model, the shear-stress transport (SST)  $k$ - $\omega$  model, was described by Menter in 1994 [34]. In this model the turbulent viscosity is modified to account for the transport of the principal turbulent shear stress. This feature gives the model an advantage in terms of performance over both the standard  $k$ - $\omega$  and  $k$ - $\varepsilon$  models. Other modifications include the addition of a cross-diffusion term in the  $\omega$  equation and the use of a blending function. Close to walls the blending function is zero, whereas remote from walls the blending function is unity and the model reverts to the standard  $k$ - $\varepsilon$  model. Hence the SST  $k$ - $\omega$  model blends the  $k$ - $\omega$  model, which is superior in the near-wall region, with the  $k$ - $\varepsilon$  model, which is less sensitive to the level of turbulence in the free stream.

Fluent provides both the original  $k$ - $\omega$  model as well as the SST  $k$ - $\omega$  model and also provides each of these models as low-Reynolds number models (fine grids) as well as high-Reynolds number models (coarse grids). Only the low-Reynolds number SST  $k$ - $\omega$  model has been used in this report as this represents the most refined version of the model to date. The simulation was performed using the grid described in the previous section to ensure maximum resolution in the near wall region. The model constants used for this particular implementation are:  $\alpha^*_{\infty} = 1$ ,  $\alpha_{\infty} = 0.52$ ,  $\alpha_0 = 1/9$ ,  $\beta^*_{\infty} = 0.09$ ,  $\beta_i = 0.072$ ,  $R_{\beta} = 8$ ,  $R_k = 6$ ,  $R_{\omega} = 2.95$ ,  $\zeta^* = 1.5$ ,  $M_{t0} = 0.25$ ,  $\sigma_k = 2.0$ ,  $\sigma_{\omega} = 2.0$ .

Figures 41 through 45 show a comparison between the simulated and experimental values of  $U/U_{ref}$  versus  $Y/T$  at selected  $X/T$  values. The level of agreement between simulation and experiment is again noticeably better than that shown by the Realizable  $k$ - $\varepsilon$  model but perhaps not quite as good as that shown by the full RSM model. The calculated results appear on average to have the same level of agreement with experiment as those calculated by either the V2F model or the Spalart-Allmaras model.

Figures 46 through 48 compare the simulated and experimental values for  $V/U_{ref}$  versus  $Y/T$  and the results show a similar trend to those shown by the  $U/U_{ref}$  calculations; the simulated results are again better than those calculated by using the Realizable  $k$ - $\varepsilon$  model but not as accurate as those calculated using the full RSM model. The level of accuracy again seems to be similar to that obtained when using either the V2F model or the Spalart-Allmaras model.

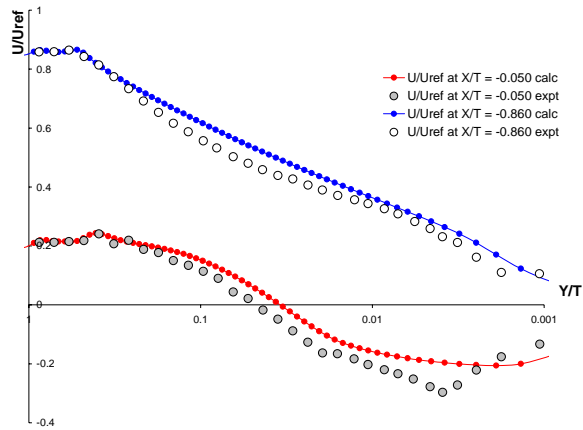


Figure 41. Comparison of simulated and experimental values of  $U/U_{ref}$  versus  $Y/T$  at  $X/T = -0.050$  and  $X/T = -0.860$  for the SST  $k-\omega$  model

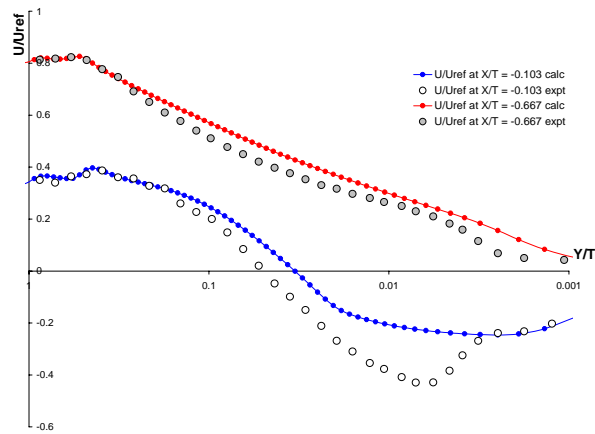


Figure 42. Comparison of simulated and experimental values of  $U/U_{ref}$  versus  $Y/T$  at  $X/T = -0.103$  and  $X/T = -0.667$  for the SST  $k-\omega$  model.

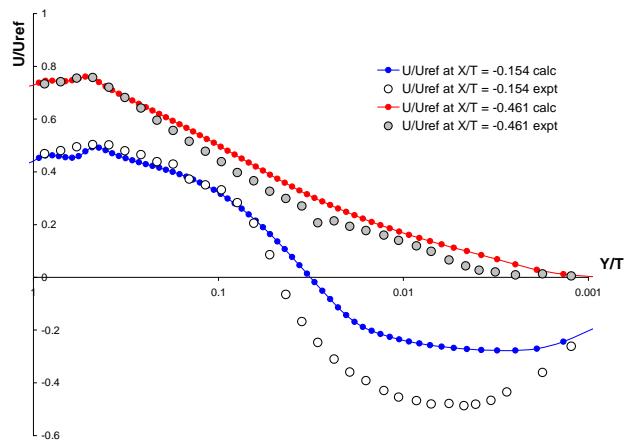


Figure 43. Comparison of simulated and experimental values of  $U/U_{ref}$  versus  $Y/T$  at  $X/T = -0.154$  and  $X/T = -0.461$  for the SST  $k-\omega$  model.

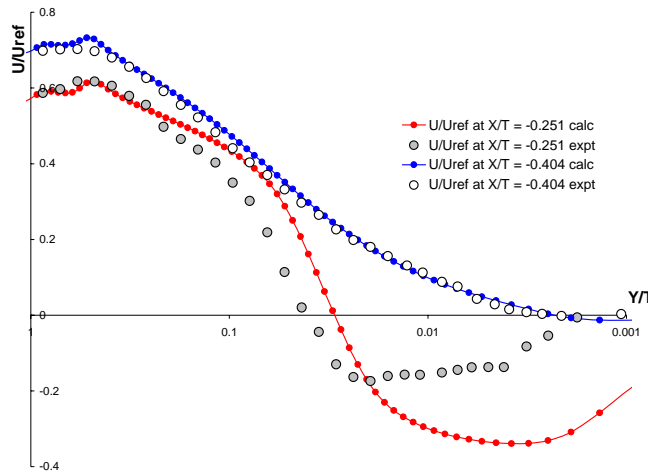


Figure 44. Comparison of simulated and experimental values of  $U/U_{ref}$  versus  $Y/T$  at  $X/T = -0.251$  and  $X/T = -0.404$  for the SST  $k-\omega$  model.

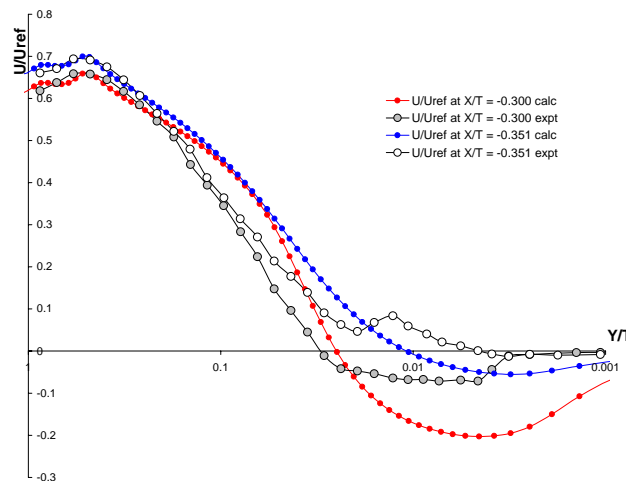


Figure 45. Comparison of simulated and experimental values of  $U/U_{ref}$  versus  $Y/T$  at  $X/T = -0.300$  and  $X/T = -0.351$  for the SST  $k-\omega$  model.

Figure 49 shows the simulated and experimental values of the turbulent kinetic energy as a function of  $Y/T$  for the same  $X/T$  locations shown in Figure 14 for the Realizable  $k-\epsilon$  model, Figure 23 for the RSM model and Figure 32 for the V2F model. Given that the SST  $k-\omega$  model was designed to be integrated through the viscous sublayer the results here are disappointing; the simulated result at  $X/T = -0.050$  is worse than that calculated by any of the other models and the results at  $X/T = -0.351$  and  $-0.860$  are comparable to those calculated using any of the other models. The simulated results still show the same incorrect trend, with the peak turbulent kinetic energy occurring closest to the wall, rather than at the vortex centre.

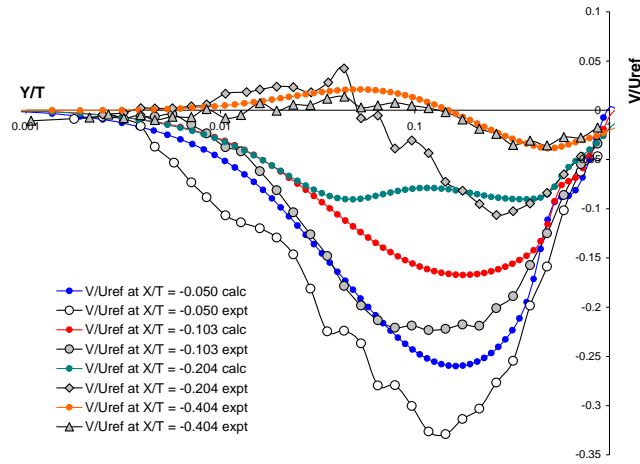


Figure 46. Comparison of simulated and experimental values of  $V/U_{ref}$  versus  $Y/T$  at selected  $X/T$  values for the SST  $k-\omega$  model model.

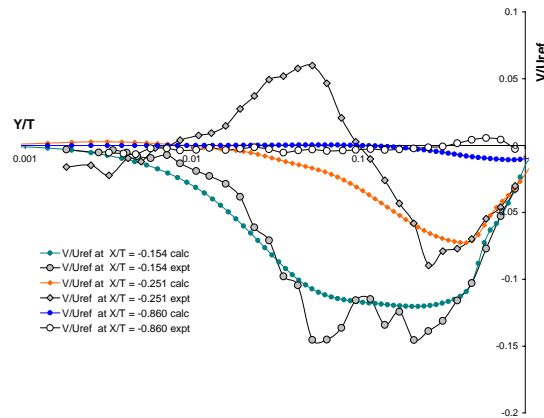


Figure 47. Comparison of simulated and experimental values of  $V/U_{ref}$  versus  $Y/T$  at selected  $X/T$  values for the SST  $k-\omega$  model model.

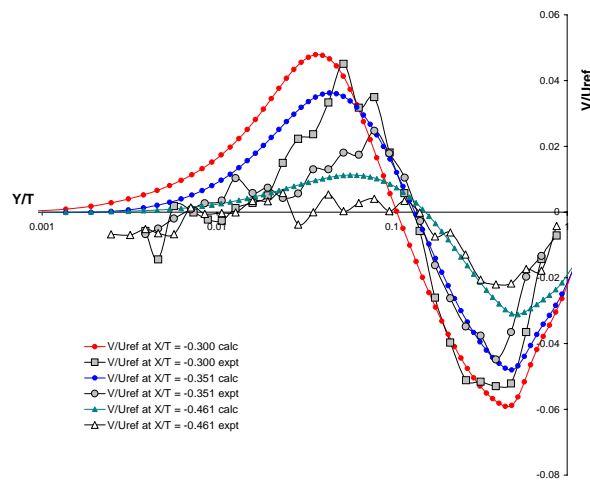


Figure 48. Comparison of simulated and experimental values of  $V/U_{ref}$  versus  $Y/T$  at selected  $X/T$  values for the SST  $k-\omega$  model.

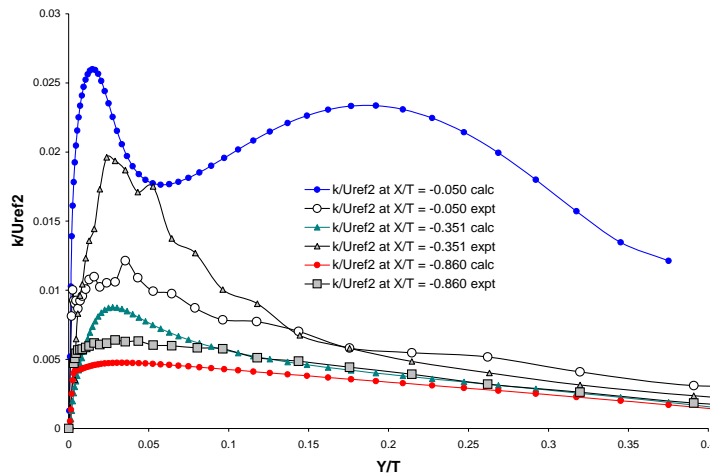


Figure 49. Comparison of simulated and experimental values of  $k/U_{ref}^2$  versus  $Y/T$  at selected  $X/T$  values for the SST  $k-\omega$  model.

## 8. Grid Independence

To ensure that the results presented in the previous sections were grid independent, simulations for each of the turbulence models were run on either two or three different grids having varying degrees of refinement. In this section we discuss the accuracy of the simulation results for each of the turbulence models separately.

Simulations using the realizable  $k-\varepsilon$  model were performed on both the second mesh described in Section 6.0 (henceforth referred to as the coarse grid) and the mesh described in Section 7.4, which was constructed for the Spalart-Allmaras model (which will be referred to as the fine mesh).

Figures 50 and 51 show plots of  $U/U_{ref}$  and  $V/U_{ref}$  as a function of  $Y/T$  at several representative  $X/T$  locations for simulations performed on both the coarse and fine meshes. Figure 50 shows that the  $U/U_{ref}$  velocity profiles calculated on the two meshes are identical, even in the highly turbulent region near the vortex core, i.e. at  $X/T = -0.300$ . The  $V/U_{ref}$  velocity profiles shown in Figure 51 however show that grid independence has not been completely achieved. The profiles at  $X/T = -0.050$  and  $X/T = -0.103$  for example, while very similar, show differences of up to 10% at certain  $Y/T$  locations. Strangely enough the profiles closer to the vortex core, for example at  $X/T = -0.154$ , are again almost identical. To achieve complete grid independence for this model would probably require a finer mesh than that described in Section 7.4. Such a mesh would be expected to improve the accuracy of the simulations by only a few percent however, and the experimental values shown in Figure 51 for  $X/T = -0.050$  and  $X/T = -0.103$  show that improvements to the simulated results of this order would have little effect on the overall agreement between the simulated and experimental results. We conclude that the results presented in Section 7.1 for the realizable  $k-\varepsilon$  model show sufficient grid independence as to make the results representative of the degree of agreement between simulation and experiment which can be achieved using this model.

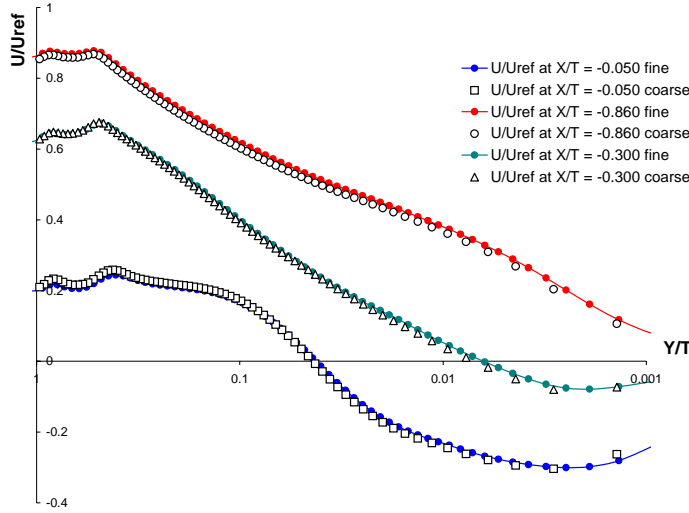


Figure 50. Plots of  $U/U_{ref}$  versus  $Y/T$  at selected  $X/T$  locations for simulations on the coarse and fine meshes for the realizable  $k-\varepsilon$  model.

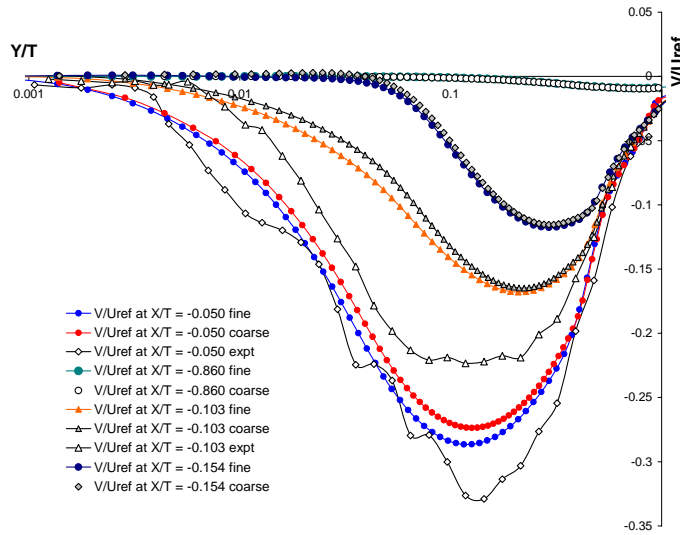


Figure 51. Plots of  $V/U_{ref}$  versus  $Y/T$  at selected  $X/T$  locations for simulations on the coarse and fine meshes for the realizable  $k-\varepsilon$  model.

For the V2F model simulations were performed on both the coarse and fine grids and comparisons between the results obtained on both grids are shown in Figures 52 and 53, which show plots of  $U/U_{ref}$  and  $V/U_{ref}$  respectively versus  $Y/T$  at selected  $X/T$  locations. Figure 52 shows that the  $U/U_{ref}$  velocity profiles calculated on the two meshes are virtually identical. There is a very slight difference in the region of the vortex centre, near  $X/T = -0.300$ , but this only on the order of a few percent. The  $V/U_{ref}$  velocity profiles in Figure 53 show a similar degree of convergence as that achieved using the realizable  $k-\varepsilon$  model. Away from the vortex centre the simulated velocity profiles on the two grids are almost identical, but at  $X/T = -0.300$  there is again a difference of a few percent over part of the  $Y/T$  range. Although the simulated profiles on the coarse and fine meshes are not identical everywhere the differences are no more than a few percent in isolated



regions and are certainly significantly less than the scatter in the experimental data in these regions, and so we conclude that the results shown in Section 7.3 for the V2F model are again representative of the degree of agreement between simulation and experiment which can be achieved using this model.

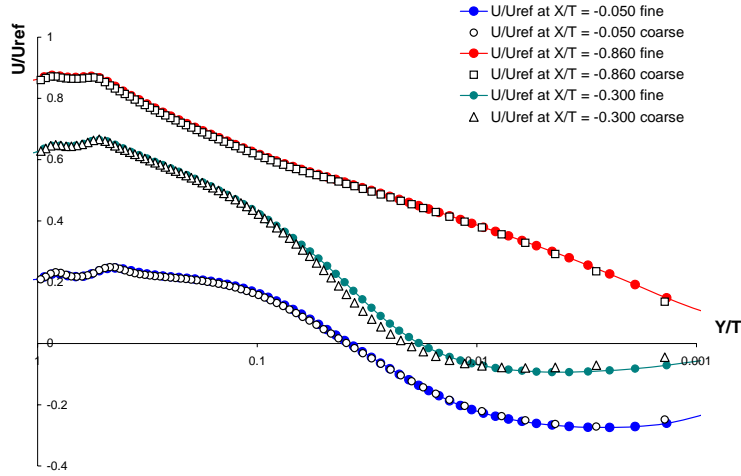


Figure 52. Plots of  $U/U_{ref}$  versus  $Y/T$  at selected  $X/T$  locations for simulations on the coarse and fine meshes for the V2F model.

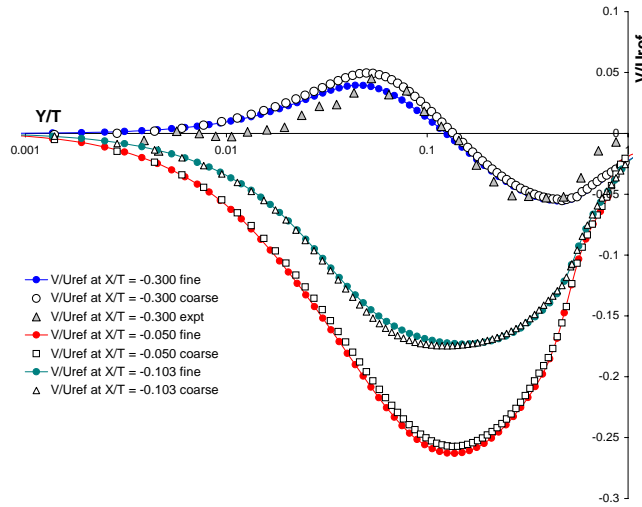


Figure 53. Plots of  $V/U_{ref}$  versus  $Y/T$  at selected  $X/T$  locations for simulations on the coarse and fine meshes for the V2F model.

Figures 54 and 55 show plots of  $U/U_{ref}$  and  $V/U_{ref}$  versus  $Y/T$  at selected  $X/T$  locations for the Spalart-Allmaras model. For this model simulations were run on three different grids; the coarse and fine grids referred to previously, as well as an even finer grid which was obtained from the fine grid using the Fluent grid adaption feature. Using the hanging node method cells marked for refinement are refined by isotropically subdividing each cell, so that a hexahedral cell for example is split into eight equivalent hexahedra. Cells can be marked for refinement using a number of criteria, but in this case, knowing the location of the vortex, the cells were refined in a region which completely encapsulated the vortical flow. This effectively doubled the number of cells in the mesh, from approximately 1 million hexahedral cells to approximately 2 million cells.

From the plots shown in Figure 54 it could be concluded that grid convergence has been achieved on the fine mesh, but inspection of the velocity profiles in Figure 55 show that there are very small differences between the profiles calculated on the fine and adapted meshes over part of the  $Y/T$  ranges for some of the  $X/T$  locations. These again occur very close to the vortex core, at  $X/T = -0.204$  for example. Elsewhere there is excellent agreement between the profiles calculated on the three different grids. Considering the level of agreement between the experimental results and the  $V/U_{ref}$  velocity profiles shown in Figures 38 to 40 however it was considered that further grid refinement in the region of the vortex core was unnecessary as it was unlikely to significantly increase the overall level of agreement between the simulated and the experimental results for the Spalart-Allmaras model.

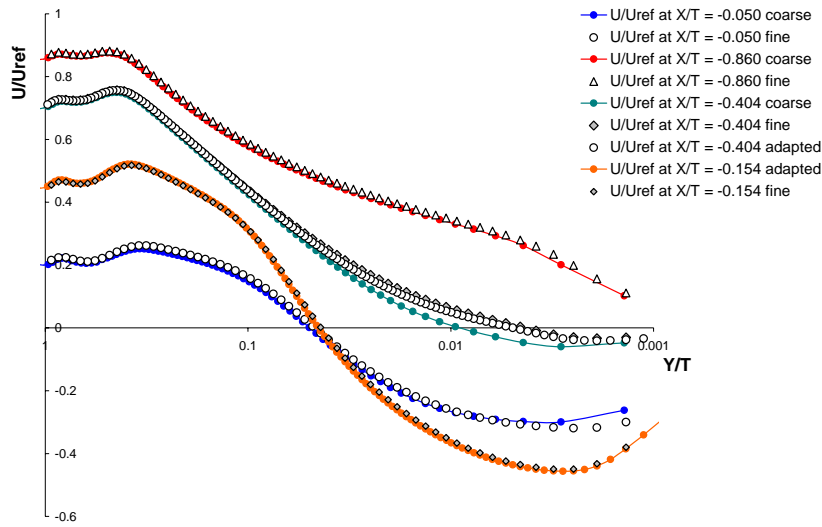


Figure 54. Plots of  $U/U_{ref}$  versus  $Y/T$  at selected  $X/T$  locations for simulations on the coarse, fine and adapted meshes for the Spalart-Allmaras model.

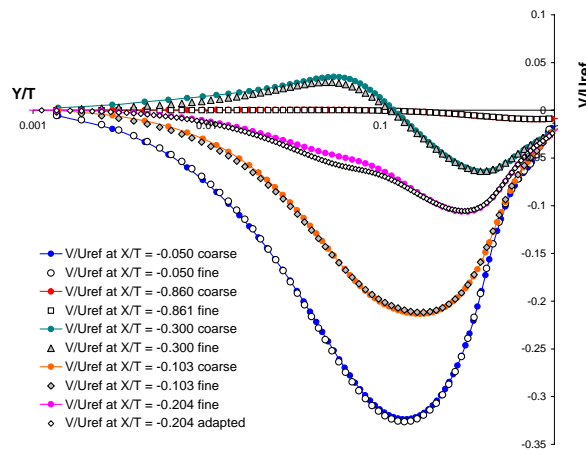


Figure 55. Plots of  $V/U_{ref}$  versus  $Y/T$  at selected  $X/T$  locations for simulations on the coarse, fine and adapted meshes for the Spalart-Allmaras model.

For the  $k-\omega$  model simulations were performed on the fine mesh and the adapted mesh described in the preceeding paragraphs. Figure 56 shows plots of  $U/U_{ref}$  versus  $Y/T$  at  $X/T = -0.050$ ,  $X/T = -0.404$  and  $X/T = -0.860$  and the profiles calculated on the two grids are identical. Figure 57 shows plots of  $U/U_{ref}$  versus  $Y/T$  at  $X/T = -0.154$  and  $X/T = -0.251$ . At  $X/T = -0.154$  the profiles on the two different meshes are again identical, but at  $X/T = -0.251$  there are differences of a few percent at the smallest  $Y/T$  values. Examination of the experimental data at this  $X/T$  station however shows that there is little point in further refining the grid in this region as the velocity profile simulated on this even finer grid would be unlikely to provide significant improvement in the agreement between the simulated and experimental data.

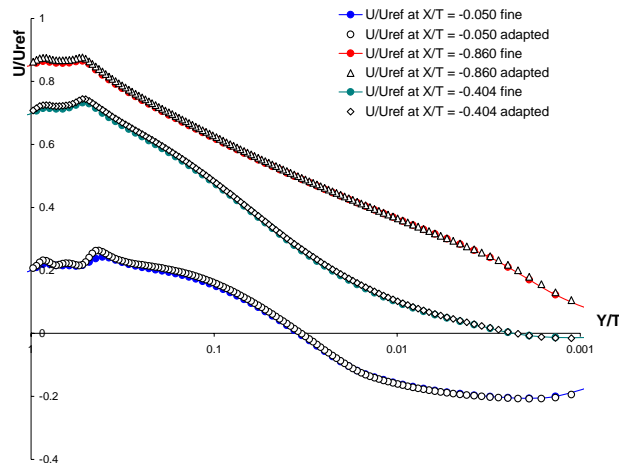


Figure 56. Plots of  $U/U_{ref}$  versus  $Y/T$  at selected  $X/T$  locations for simulations on the fine and adapted meshes for the  $k-\omega$  model

Figure 58 for the plots of  $V/U_{ref}$  versus  $Y/T$  at  $X/T = -0.050$ ,  $X/T = -0.154$ ,  $X/T = -0.300$  and  $X/T = -0.404$  shows a similar trend. There is excellent agreement between the velocity profiles calculated on the two grids for  $X/T = -0.050$ ,  $X/T = -0.154$  and  $X/T = -0.404$ , but at  $X/T = -0.300$  there is a significant difference between the profiles over a considerable part of the  $Y/T$  range. Again, examination of the experimental data for this  $X/T$  location shows that further grid refinement in this region is unlikely to significantly improve the agreement between the simulated and experimental data.

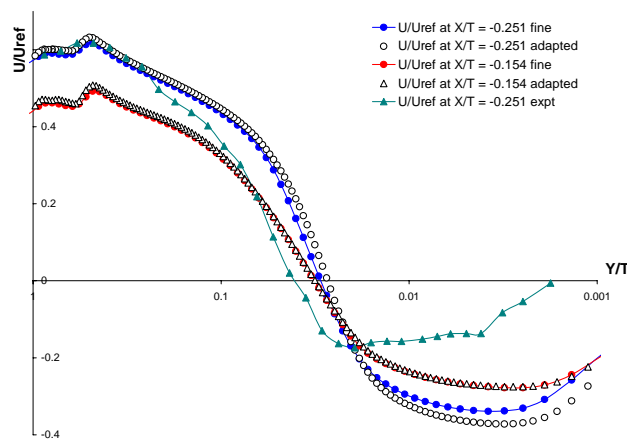


Figure 57. Plots of  $U/U_{ref}$  versus  $Y/T$  at selected  $X/T$  locations for simulations on the fine and adapted meshes for the  $k-\omega$  model

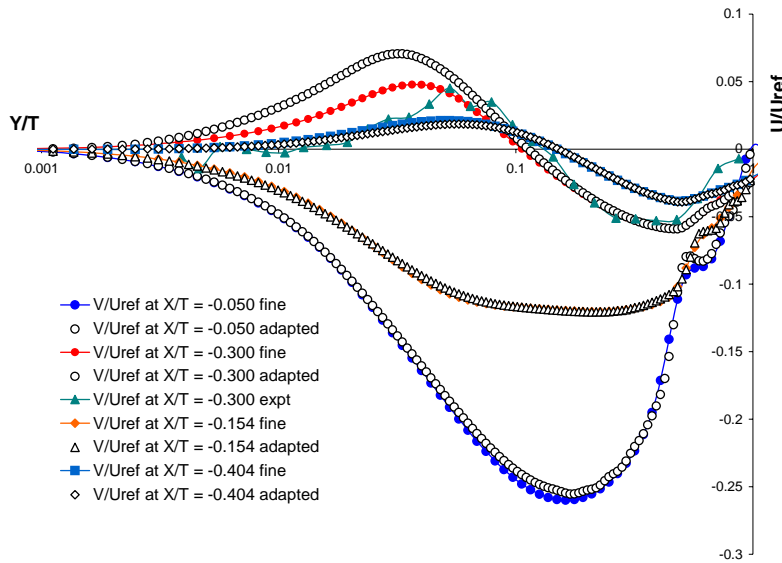


Figure 58. Plots of  $V/U_{ref}$  versus  $Y/T$  at selected  $X/T$  locations for simulations on the fine and adapted meshes for the  $k-\omega$  model

The simulations on the different meshes presented so far in this section have demonstrated effective grid convergence for both the realizable  $k-\varepsilon$  model and the V2F model on the coarse mesh, and for the Spalart-Allmaras model and the  $k-\omega$  model on the fine mesh. For the RSM model however the situation is more complex. Figures 59 through 66 show simulations for the RSM model on both the coarse and fine meshes using both non-equilibrium wall functions as well as advanced wall functions. Both wall functions were trialed because the Fluent 6.0 User's Guide states "Using the RSM creates a high degree of coupling between the momentum equations and the turbulent stresses in the flow, and thus the calculation can be more prone to stability and convergence difficulties than with the  $k-\varepsilon$  models." [35]. The following recommendation is also noted "When calculating with RSM it is recommended that the Non-Equilibrium Wall Functions are used" [36]. Whilst the reason for this recommendation was not given, it was certainly noted that convergence of the RSM on both the coarse and fine mesh was easily obtained using non-equilibrium wall functions, while convergence on any mesh using enhanced wall functions was extremely difficult to obtain. Also, it should be noted that much better convergence from the point of view of residuals was obtained using non-equilibrium wall functions. On either the coarse or fine grid the residuals were observed to reduce by up to six orders of magnitude using the non-equilibrium wall functions, whilst when using the enhanced wall functions the residuals typically reduced by only three orders of magnitude and then the calculation became unstable. Hence, whilst a calculation using enhanced wall functions on the fine grid might be expected to give superior results to a calculation on the coarse grid using non-equilibrium wall functions, this is not necessarily the case because of the poor convergence (from the residuals view point) of the calculation on the fine mesh using enhanced wall functions.

Examination of Figures 59 through 66 shows some interesting features. For many of the  $X/T$  locations away from the centre of the vortex, for example at  $X/T = -0.050$ ,  $-0.103$ ,  $-0.154$  and  $-0.860$  there is fairly good agreement between simulations performed on the coarse and fine grids using the non-equilibrium wall functions and those on the fine grid using the enhanced wall functions. Even at  $X/T = -0.204$  and  $-0.404$  the agreement between these three simulations is still reasonable. Only at  $X/T = -0.300$  for  $U/U_{ref}$  and at  $X/T = -0.251$  for  $V/U_{ref}$  are there significant differences

between the three simulations. In both these cases however it is interesting to note that the experimental results agree more closely with the simulation performed on the coarse mesh using the non-equilibrium wall functions. This was also found to be the case at other  $X/T$  locations. These simulations are obviously not fully converged, but pursuing convergence on more and more refined grids using non-equilibrium wall functions is questionable in any case, and it is also not apparent that convergence can be obtained using enhanced wall functions. For these reasons the results presented in Section 7.2 use the simulations performed on the coarse mesh using the non-equilibrium wall functions.

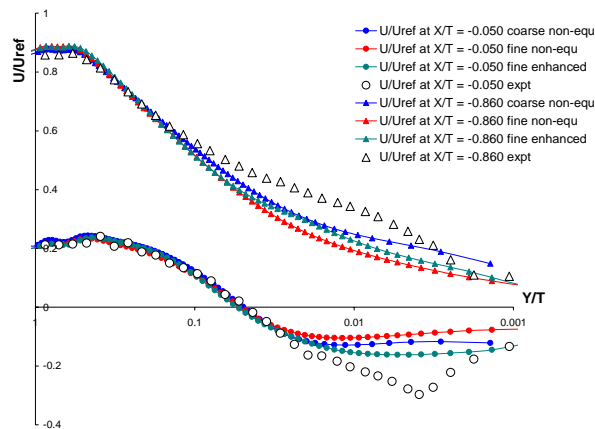


Figure 59. Plots of  $U/U_{ref}$  versus  $Y/T$  at  $X/T = -0.050$  and  $X/T = -0.860$  for simulations on the coarse and fine meshes for the RSM model.

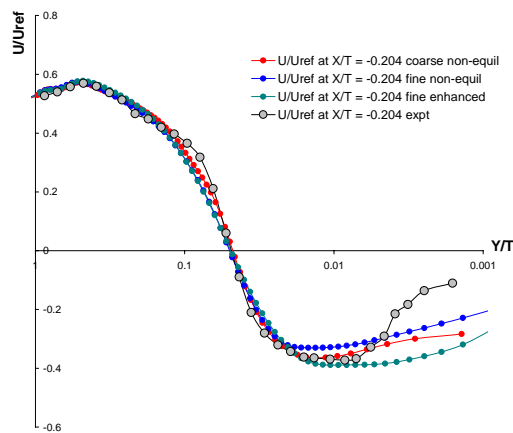


Figure 60. Plots of  $U/U_{ref}$  versus  $Y/T$  at  $X/T = -0.204$  for simulations on the coarse and fine meshes for the RSM model.

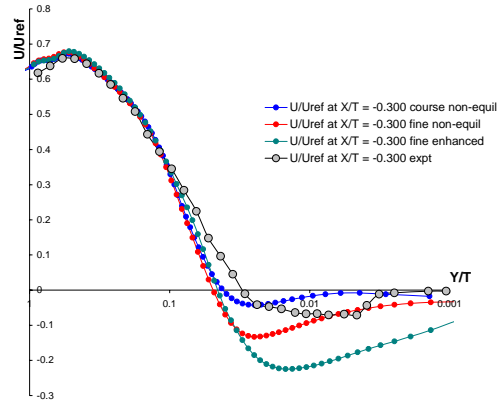


Figure 61. Plots of  $U/U_{ref}$  versus  $Y/T$  at  $X/T = -0.300$  for simulations on the coarse and fine meshes for the RSM model.

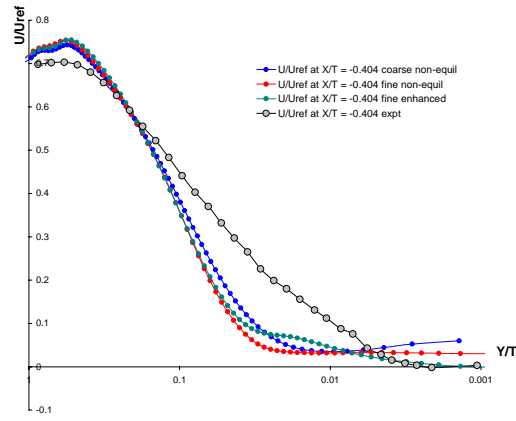


Figure 62. Plots of  $U/U_{ref}$  versus  $Y/T$  at  $X/T = -0.404$  for simulations on the coarse and fine meshes for the RSM model.

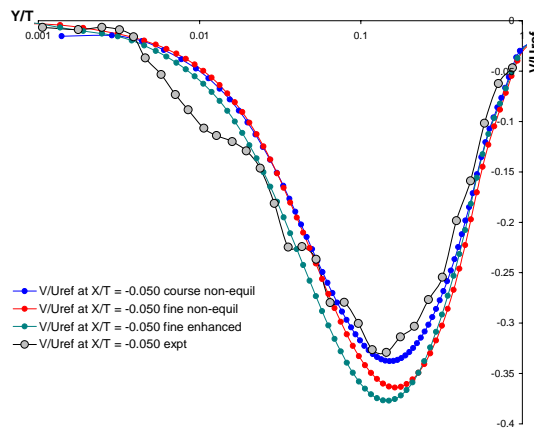


Figure 63. Plots of  $V/U_{ref}$  versus  $Y/T$  at  $X/T = -0.050$  for simulations on the coarse and fine meshes for the RSM model.

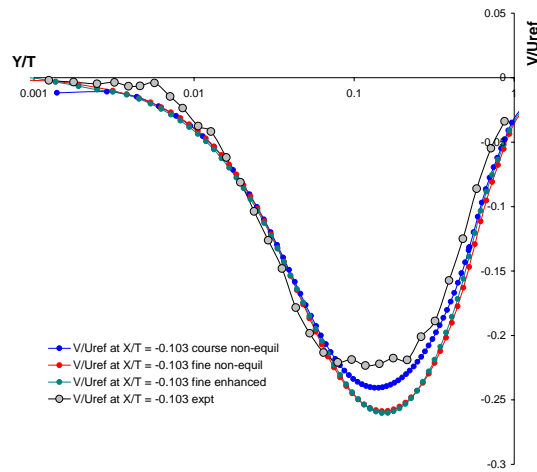


Figure 64. Plots of  $V/U_{ref}$  versus  $Y/T$  at  $X/T = -0.103$  for simulations on the coarse and fine meshes for the RSM model.

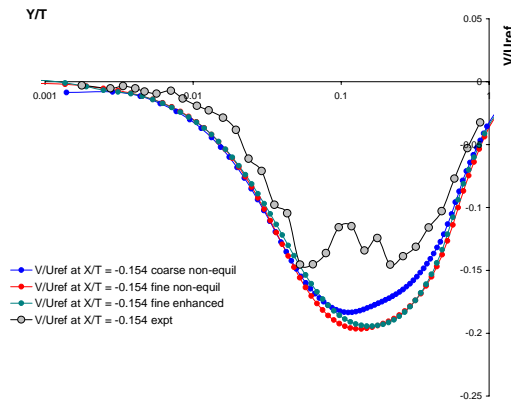


Figure 65. Plots of  $V/U_{ref}$  versus  $Y/T$  at  $X/T = -0.154$  for simulations on the coarse and fine meshes for the RSM model.

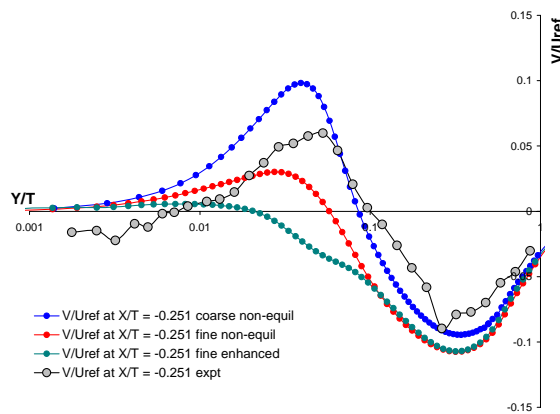


Figure 66. Plots of  $V/U_{ref}$  versus  $Y/T$  at  $X/T = -0.251$  for simulations on the coarse and fine meshes for the RSM model.

## 9. Discussion and Conclusion

The aim of this report was to investigate and document the accuracy with which the Fluent CFD code and the various turbulence models contained within it could simulate the horseshoe vortex formed in the Devenport-Simpson experiment [4]. Simulations were conducted using each of the turbulence models and the calculated results were compared with experimental results obtained from an extensive database of results available at the University of Surrey's website [3]. In all cases comparisons were made in the plane of symmetry upstream of the wing for the mean components of velocity in the direction of the free-stream and normal to the flat plate at eleven stations upstream of the wing, as well as the pressure distribution along the surface of the wing at selected locations.

All of the calculations accurately reproduced the pressure distributions around the wing and only results for the  $k-\varepsilon$  model were presented as the remaining models displayed identical results, which was as expected. The mean velocity components in the free-stream direction and normal to the flat plate were reasonably well simulated by all the turbulence models, except in the vicinity of the vortex core. The realizable  $k-\varepsilon$  model and the Spalart-Allmaras model were less accurate than the other models in simulating velocity components in the vortex core, while the remaining models, the RSM, the V2F model and the  $k-\omega$  model all displayed similar levels of accuracy with regard to simulations of the mean velocity components in the vortex core. None of the models was able to accurately simulate the correct trend for the behaviour of the mean kinetic energy as a function of  $Y/T$  at selected  $X/T$  values. Experimentally the peak value of the turbulent kinetic energy occurs close to the centre of the vortex, while all the simulated results showed a different trend, with the kinetic energy increasing continuously as the distance to the wing decreased, with the maximum value occurring not at the vortex centre but at the closest point to the wing surface. The V2F model however came closest to predicting the correct behaviour close to the wall. This is similar to the result found by Parneix et al. [11].

Apsley and Leschziner [10] noted that RSM offered predictive advantages over other models examined in their study, especially in terms of the far-field structure of the horseshoe vortex. Chen [13] also found that the RSM gave a superior performance over that of the simpler isotropic eddy viscosity model. In contrast to this, Rodi et al. [12] found that the RSM and intermediate algebraic-stress and non-linear  $k-\varepsilon$  models were no better than the simpler linear eddy viscosity models for the practically relevant mean quantities. Our own conclusion is that the RSM in Fluent can be particularly unstable and that convergence can be difficult to achieve. Despite this, the results shown in Section 7.2 calculated using non-equilibrium wall functions on the coarse grid, even though not fully converged, show agreement with experiment as good as that obtained using the V2F, Spalart-Allmaras or  $k-\omega$  model. The RSM is computationally more expensive than any of the other models however. Both the Spalart-Allmaras and  $k-\omega$  models require fine resolution close to any boundaries, and this can also lead to computationally expensive simulations compared to either the  $k-\varepsilon$  model or the V2F model. Based on the above considerations, it would appear that the V2F model offers the best combination of computational accuracy, computational efficiency, and ease of use.

## 10. Acknowledgements

We would like to thank Michael Roomina of Fluvius Pty. Ltd. (distributors of Fluent within Australia) for arranging the use of a complimentary licence for the V2F model during the course of this work, as well as for many helpful insights on several aspects of these simulations.



## 11. References

1. Fluent – Commercially available CFD software package based on the Finite Volume method. A product of Fluent Inc., Centerra Resource Park, 10 Cavendish Court, Lebanon, NH, USA. Distributed in Australia by Fluvius Pty. Ltd.
2. CFX– Commercially available CFD software package based on the Finite Volume method. A product of AEA Technology Engineering Software, Didcot, Oxfordshire, UK. Distributed in Australia by ATD International Pty. Ltd., Hawthorn, Vic.
3. Available at the web site <http://vortex.mech.surrey.ac.uk>.
4. Devenport, W.J. and Simpson, R.L., "Time-dependent and time-averaged turbulence structure near the nose of a wing-body junction", *J. Fluid Mech.* **210**, 23-55, (1990).
5. Fleming, J.L., Simpson, R.L., Cowling, J.E. and Devenport, W.J., "An experimental study of wing-body junction and wake flow", *Exp. Fluids*, **14**, 366-378, (1993).
6. Olcman, M.S. and Simpson, R.L., "Some Features of a Turbulent Wing-Body Vortical Flow", AIAA Paper #97-0651, AIAA 35<sup>th</sup> Aerospace Sciences Meeting, Reno, NV, January 1997.
7. Devenport, W.J., Simpson, R.L., Dewitz, M.B. and Agarwal, N.K., "Effects of a Leading-Edge Fillet on the Flow Past an Appendage-Body Junction", AIAA Paper #91-0252, AIAA 29<sup>th</sup> Aerospace Sciences Meeting, Reno, NV, January 1991.
8. Anderson, B. and Huyer, S.A., "Sail-Junction Vortex Experiment", NUWC, Newport, Rhode Island, July/April 2002.
9. Simpson, R.L., "Junction Flows", *Annual. Rev. Fluid Mech.* **33**, 415-443, (2001).
10. Apsley, D.D. and Leschziner, M.A., "Investigation of Advanced Turbulence Models for the Flow in a Generic Wing-Body Junction", *Flow, Turbulence and Combustion*, **67**, 25-55 (2001).
11. Parneix, S., Durbin, P.A. and Behnia, M., "Computation of 3-D Turbulent Boundary Layers Using the V2F Model", *Flow, Turbulence and Combustion*, **60**, 19-46, (1998).
12. Rodi, W., Bonnin, J.C., Buchal, T. and Laurence, D. "Testing of calculation methods for turbulent flows: Workshop results for 5 test cases", *Electricité de France Report 98NB00004* (1998).
13. Chen, H.C., "Assessment of a Reynolds Stress Closure Model for Appendage-Hull Junction Flows", *Journal of Fluids Engineering*, **117**, 557-563, (1995).
14. Speziale, C.G, Sarkar, S. and Gatski, T.B., "Modelling the Pressure-Strain Correlation of Turbulence: An Invariant Dynamical Systems Approach", *Journal of Fluid Mechanics*, **227**, 245-272, (1991).
15. Fu, S., Zhai, Z., Rung, T. and Thiele, F., "Numerical Study of Flow Past a Wing-Body Junction with a Realizable Nonlinear EVM", *Eleventh Symposium on Turbulent Shear Flows, Volume 1*, Grenoble, France, September 8-10, 1997.
16. Gatski, T.B. and Spezial, C.G., "On explicit algebraic stress models for complex turbulent flows", *Journal of Fluid Mechanics*, **254**, 59-78, (1993).
17. Fu, S., Rung, T. and Thiele, F. "On the realizability of the non-linear stress-strain relationship for Reynolds-stress closures", *Technical Report*, HFI, TU-Berlin, (1996).
18. Pope, S. B., "Turbulent Flows", Cambridge University Press, 2000.

19. Wolfstein, M., "The Velocity and Temperature Distribution of One-Dimensional Flow with Turbulence Augmentation and Pressure Gradient", *Int. J. Heat Mass Transfer*, **12**, 301-318 (1969).
20. Jones, W.P. and Launder, B.E. "The prediction of laminarization with a two-equation model of turbulence", *Int. J. Heat Mass Transfer*, **15**, 301-314 (1972).
21. Launder, B.E. and Sharma, B.I. "Application of the energy-dissipation model of turbulence to the calculation of flow near a spinning disc", *Lett. Heat Mass Transf.*, **1**, 131-138 (1974)
22. Yakhot, V. and Orszag, S.A. "Renormalization group analysis of turbulence. 1. Basic theory", *J. Sci. Comput.*, **1**, 3-51 (1986)
23. Shih, T.H, Liou, W., Shabbir, A. and Zhu, J. "A new  $k$ - $\varepsilon$  eddy- viscosity model for high Reynolds number turbulent flows - model development and validation", *Computers Fluids*, **24**, 227-238 (1995).
24. Durbin, P. "Near-Wall Turbulence Closure Modelling Without Damping Functions", *Comput. Fluid Dynamics*, **3**, 1-13 (1991).
25. Durbin, P. "A Reynolds Stress Model for Near-Wall Turbulence", *J. Fluid Mech.*, **249**, 465-498 (1993).
26. Durbin, P. "Separated Flow Computations with the  $k$ - $\varepsilon$ - $v^2$  Model", *AIAA J.*, **33**, No. 4, 659-664 (1995).
27. Parneix, S., Durbin, P. and Behnia, M. "Computation of 3D turbulent boundary layers using the  $v^2$ - $f$  model", *Flow, Turbulence and Combustion*, **10**, 19-46 (1998).
28. Durbin, P.A., "On the  $k$ - $\varepsilon$  Stagnation Point Anomaly", *Int. J. Heat and Fluid Flow*, **17**, 89-90 (1996).
29. Spalart, R.P. and Allmaras, S.R., "A one-equation turbulence model for aerodynamic flows", *La Recherche Aérospatiale*, **1**, 5-21 (1994).
30. Fluent 6.1 Tutorial Guide Number 3, "Modelling External Compressible Flow", available at [www.fluent.com](http://www.fluent.com)
31. Paciorri, R., Dieudonné, W., Degrez, G., Charbonnier, J.-M. and Deconinck, H., "Validation of the Spalart-Allmaras Turbulence Model for Application in Hypersonic Flows", *AIAA paper No. 97-2023, AIAA Fluid Dynamics Conference*, June 29 - July 2, Snowmass Village, Colorado (1997).
32. Wilcox, D.C., "Reassessment of the Scale Determining Equation for Advanced Turbulence Models", *AIAA Journal*, **26**, No. 11, 1299-1320 (1988).
33. Wilcox, D.C., "Turbulence Modelling for CFD", 2<sup>nd</sup> edition, DCW Industries, Inc. (1998).
34. Menter, F., "Two-equation eddy-viscosity turbulence models for engineering applications", *AIAA Journal*, **32**, 1598-1605 (1994).
35. Fluent 6.0 User's Guide Volume 2, 10-95, December 2001.
36. Some Remarks and Techniques for handling Automotive External Aerodynamic Set-up and Simulation, available at [www.fluent.com](http://www.fluent.com)
37. Patankar, S.V. and Spalding, D.B., "A Calculation Procedure for Heat, Mass and Momentum Transfer in Three-Dimensional Parabolic Flows", *Int. J. Heat Mass Transfer*, **15**, 1787 (1972)
38. Van Doormal, J.P. and Raithby, G.D. "Enhancements of the SIMPLE Method for Predicting Incompressible Fluid Flows", *Numer. Heat Transfer*, **7**, pp. 147-163, (1984)

39. Issa, R.I., Gosman, A.D. and Watkins, A.P., "The Computation of Compressible and Incompressible Recirculating Flows", *J. Comput. Phys.*, **62**, pp. 66-82 (1986)
40. Patankar, S.V. *Numerical Heat Transfer and Fluid Flow*, Hemisphere Publishing Corporation, Taylor and Francis Group, New York, (1980)
41. Leonard, B.P., "A Stable and Accurate Convective Modelling Procedure Based on Quadratic Upstream Interpolation", *Comput. Methods Appl. Mech. Eng.*, **19**, pp. 59-98, (1979)

## DISTRIBUTION LIST

### Simulation of a Wing-Body Junction Experiment using the Fluent Code

*D.A. Jones and D.B. Clarke*

## AUSTRALIA

### DEFENCE ORGANISATION

### No. of copies

#### Task Sponsor

PSO (CapDev) COMAUSNAVSUBGRP, Stirling

1

#### S&T Program

Chief Defence Scientist

FAS Science Policy

AS Science Corporate Management

Director General Science Policy Development

Counsellor Defence Science, London

Counsellor Defence Science, Washington

Scientific Adviser to MRDC, Thailand

Scientific Adviser Joint

Navy Scientific Adviser

Scientific Adviser – Army

Shared

Doc Data Sheet

Doc Data Sheet

Doc Data Sheet

Doc Data Sheet

1

Doc Data Sht & Dist  
List

Doc Data Sht & Dist  
List

Doc Data Sht & Dist  
List

#### Platforms Sciences Laboratory

Director of PSL

Doc Data Sht & Exec  
Summ

Chief of Maritime Platforms Division

Doc Data Sht & Dist  
List

Ms. Janis Cocking

Doc Data Sht & Dist  
List

Task Manager: Mr. B. Anderson

5

Author(s): Dr. D.A. Jones

5

Mr. D.B. Clarke

1

#### DSTO Library and Archives

Library Fishermans Bend

Doc Data Sheet

Library Edinburgh

1

Defence Archives

1

#### Capability Development Group

Director General Maritime Development

Doc Data Sheet

Director General Capability and Plans

Doc Data Sheet

Assistant Secretary Investment Analysis	Doc Data Sheet
Director Capability Plans and Programming	Doc Data Sheet
Director General Australian Defence Simulation Office	Doc Data Sheet

### **Chief Information Officer Group**

Director General Australian Defence Simulation Office	Doc Data Sheet
Director General Information Policy and Plans	Doc Data Sheet
AS Information Strategy and Futures	Doc Data Sheet
AS Information Architecture and Management	Doc Data Sheet
Director General Information Services	Doc Data Sheet

### **Strategy Group**

Director General Military Strategy	Doc Data Sheet
Assistant Secretary Strategic Policy	Doc Data Sheet
Assistant Secretary Governance and Counter-Proliferation	Doc Data Sheet

### **Navy**

Maritime Operational Analysis Centre, Building 89/90 Garden Island Sydney NSW	Doc Data Sht & Dist List
Deputy Director (Operations)	
Deputy Director (Analysis)	
Director General Navy Capability, Performance and Plans, Navy Headquarters	Doc Data Sheet
Director General Navy Strategic Policy and Futures, Navy Headquarters	Doc Data Sheet

### **Air Force**

SO (Science) - Headquarters Air Combat Group, RAAF Base, Williamstown NSW 2314	Doc Data Sht & Exec Summ
---	-----------------------------

### **Army**

#### **ABCA National Standardisation Officer**

Land Warfare Development Sector, Puckapunyal	e-mailed Doc Data Sheet
SO (Science) - Land Headquarters (LHQ), Victoria Barracks NSW	Doc Data & Exec Summary
SO (Science), Deployable Joint Force Headquarters (DJFHQ) (L), Enoggera QLD	Doc Data Sheet

### **Joint Operations Command**

Director General Joint Operations	Doc Data Sheet
Chief of Staff Headquarters Joint Operations Command	Doc Data Sheet
Commandant ADF Warfare Centre	Doc Data Sheet
Director General Strategic Logistics	Doc Data Sheet
COS Australian Defence College	Doc Data Sheet

### **Intelligence and Security Group**

AS Concepts, Capability and Resources	1
DGSTA , DIO	1
Manager, Information Centre, Defence Intelligence Organisation	1 (PDF)
Assistant Secretary Capability Provisioning	Doc Data Sheet

Assistant Secretary Capability and Systems	Doc Data Sheet
--	----------------

**Defence Materiel Organisation**

Deputy CEO	Doc Data Sheet
Head Aerospace Systems Division	Doc Data Sheet
Head Maritime Systems Division	Doc Data Sheet
Head Electronic and Weapon Systems Division	Doc Data Sheet
Program Manager Air Warfare Destroyer	Doc Data Sheet

**Defence Libraries**

Library Manager, DLS-Canberra	Doc Data Sheet
-------------------------------	----------------

**OTHER ORGANISATIONS**

National Library of Australia	1
NASA (Canberra)	1
Library of New South Wales	1
State Library of South Australia	1

**UNIVERSITIES AND COLLEGES**

**Australian Defence Force Academy**

Library	1
Head of Aerospace and Mechanical Engineering	1
Serials Section (M list), Deakin University Library, Geelong, VIC	1
Hargrave Library, Monash University	Doc Data Sheet
Librarian, Flinders University	1

**OUTSIDE AUSTRALIA**

**INTERNATIONAL DEFENCE INFORMATION CENTRES**

US Defense Technical Information Center	1 PDF
UK Dstl Knowledge Services	1 PDF
Canada Defence Research Directorate R&D Knowledge & Information Management (DRDKIM)	1
NZ Defence Information Centre	1

**ABSTRACTING AND INFORMATION ORGANISATIONS**

Library, Chemical Abstracts Reference Service	1
Engineering Societies Library, US	1
Materials Information, Cambridge Scientific Abstracts, US	1
Documents Librarian, The Center for Research Libraries, US	1

**INFORMATION EXCHANGE AGREEMENT PARTNERS**

National Aerospace Laboratory, Japan	1
National Aerospace Laboratory, Netherlands	1

SPARES	5
--------	---

<b>Total number of copies:</b>	<b>Printed: 43</b>	<b>PDF: 3</b>
--------------------------------	--------------------	---------------

<b>DEFENCE SCIENCE AND TECHNOLOGY ORGANISATION</b>  <b>DOCUMENT CONTROL DATA SHEET</b>					
				1. PRIVACY MARKING/CAVEAT (OF DOCUMENT)	
2. TITLE  Simulation of a Wing-Body Junction Experiment <input type="checkbox"/> using the Fluent Code			3. SECURITY CLASSIFICATION (FOR UNCLASSIFIED REPORTS THAT ARE LIMITED RELEASE USE (L) NEXT TO DOCUMENT CLASSIFICATION)  Document (U) Title (U) Abstract (U)		
4. AUTHOR(S)  D.A. Jones and D.B. Clarke			5. CORPORATE AUTHOR  Platforms Sciences Laboratory 506 Lorimer St Fishermans Bend Victoria 3207 Australia		
6a. DSTO NUMBER DSTO-TR-1731		6b. AR NUMBER AR-013-426		6c. TYPE OF REPORT Technical Report	
				7. DOCUMENT DATE June 2005	
8. FILE NUMBER eg: 2005/1002854/1		9. TASK NUMBER NAV 03/136		10. TASK SPONSOR CANSNG	
				11. NO. OF PAGES 52	
				12. NO. OF REFERENCES 42	
13. URL on the World Wide Web  <a href="http://www.dsto.defence.gov.au/corporate/reports/DSTO-TR-1731.pdf">http://www.dsto.defence.gov.au/corporate/reports/DSTO-TR-1731.pdf</a>				14. RELEASE AUTHORITY  Chief, Maritime Platforms Division	
15. SECONDARY RELEASE STATEMENT OF THIS DOCUMENT  <p style="text-align: center;"><i>Approved for public release</i></p>					
OVERSEAS ENQUIRIES OUTSIDE STATED LIMITATIONS SHOULD BE REFERRED THROUGH DOCUMENT EXCHANGE, PO BOX 1500, EDINBURGH, SA 5111					
16. DELIBERATE ANNOUNCEMENT  No Limitations					
17. CITATION IN OTHER DOCUMENTS Yes					
18. DEFTEST DESCRIPTORS  Computational Fluid Dynamics, Numerical Simulation, Fluid Flow, Turbulence, Horseshoe Vortex					
19. ABSTRACT Numerical simulations are performed using the Fluent Computational Fluid Dynamics code and the various turbulence models to simulate the horseshoe vortex formed in a typical wing-junction turbulent flow experiment. Simulations were conducted using the renormalizable $k-\varepsilon$ model, the Reynolds Stress Model, the V2F model, the Spalart-Allmaras model and the $k-\omega$ model. The calculated results were compared with experimental results obtained from an extensive database available on the internet [3]. The realizable $k-\varepsilon$ model was noticeably less accurate than all other models in simulating the mean velocity components, while the remaining models all displayed similar levels of accuracy. None of the models were able to accurately simulate the correct behaviour of the mean kinetic energy as a function of position. The V2F model however came closest to predicting the correct behaviour, and offers the best combination of computational accuracy, computational efficiency, and ease of use.					